Supplementary Information (SI) for Journal of Materials Chemistry C.

Defect–Structure–Performance Correlation in Eu^{3+}@UiO-66:

Design of Coordination Sites for Rapid Optical O_2 Sensing

*Zhenyu Zhao, and Michael Tiemann**

Paderborn University, Department of Chemistry,
Warburger Str. 100, 33098 Paderborn (Germany)

* Email: michael.tiemann@web.de

Supporting Information

Table S1. Details of Synthesis: Added number of reagents and comparison with calculated incorporation amount of fumaric acid and isophthalic acid, determined from solution ^{1}H-NMR

(a) UiO-66-x ox

Ox-Eq.	n_{ZrCl4} m_{ZrCl4}	n_{H2BDC} m_{H2BDC}	M:L	n_{HCl} v_{HCl}	n_{DMF} v_{DMF}	n_{ox} m_{ox}	M : Ox
x = 1	514.97 µmol 120 mg	669.35 µmol 111.22 mg	1:1.3	40.87 mmol 1ml	194.54 mmol 15ml	514.97 µmol 46.36mg	1:1
x = 0.75						386.19 µmol 34.77 mg	1:0.75
x = 0.5						257.46 µmol 18.77 mg	1:0.5
x = 0.25						128.73 µmol 11.759 mg	1:0.25
x = 0						/	/

(b) UiO-66-x fum

Fum-eq.	n_{ZrCl4} m_{ZrCl4}	n_{H2BDC} m_{H2BDC}	n_{HCl} v_{HCl}	n_{DMF} v_{DMF}	n_{fum} m_{fum}	n_{BDC}/n_{fum}	$(n_{BDC}/n_{fum})_{NMR}$
x = 1	514.97 µmol 120 mg	669.35 µmol 111.22 mg	40.87 mmol 1ml	194.54 mmol 15ml	514.97 µmol 59.77 mg	1:1	1:0.14
x = 0.75					386.19 µmol 44.83 mg	1:0.75	1:0.07
x = 0.5					257.46 µmol 29.89 mg	1:0.5	1:0.05
x = 0.25					128.73 µmol 14.94 mg	1:0.25	1:0.03

(c) UiO-66-x ipa

x_{ipa}	n_{ZrCl4} m_{ZrCl4}	$n_{BDC,L1}$ $m_{BDC,L1}$	$n_{ipa,L2}$ $m_{ipa,L2}$	$x_{ipa} = n_{ipc}/n_{BDC}+n_{ipc}$	$(n_{ipc}/n_{BDC}+n_{ipc})_{NMR}$	n_{HCl} v_{HCl}	n_{DMF} v_{DMF}
x = 0.75	514.97 µmol 120 mg	257.46 µmol 27.80 mg	257.46 µmol 83.41 mg	0.75	4	40.87 mmol 1ml	194.54 mmol 15ml
x = 0.5		334.73 µmol 55.61 mg	334.73 µmol 55.61 mg	0.5	0.38		
x = 0.25		257.46 µmol 83.41 mg	257.46 µmol 27.80 mg	0.25	0.15		
x = 0.1		590.49 µmol 98.10 mg	74.64 µmol 12.40 mg	0.1	0.07		

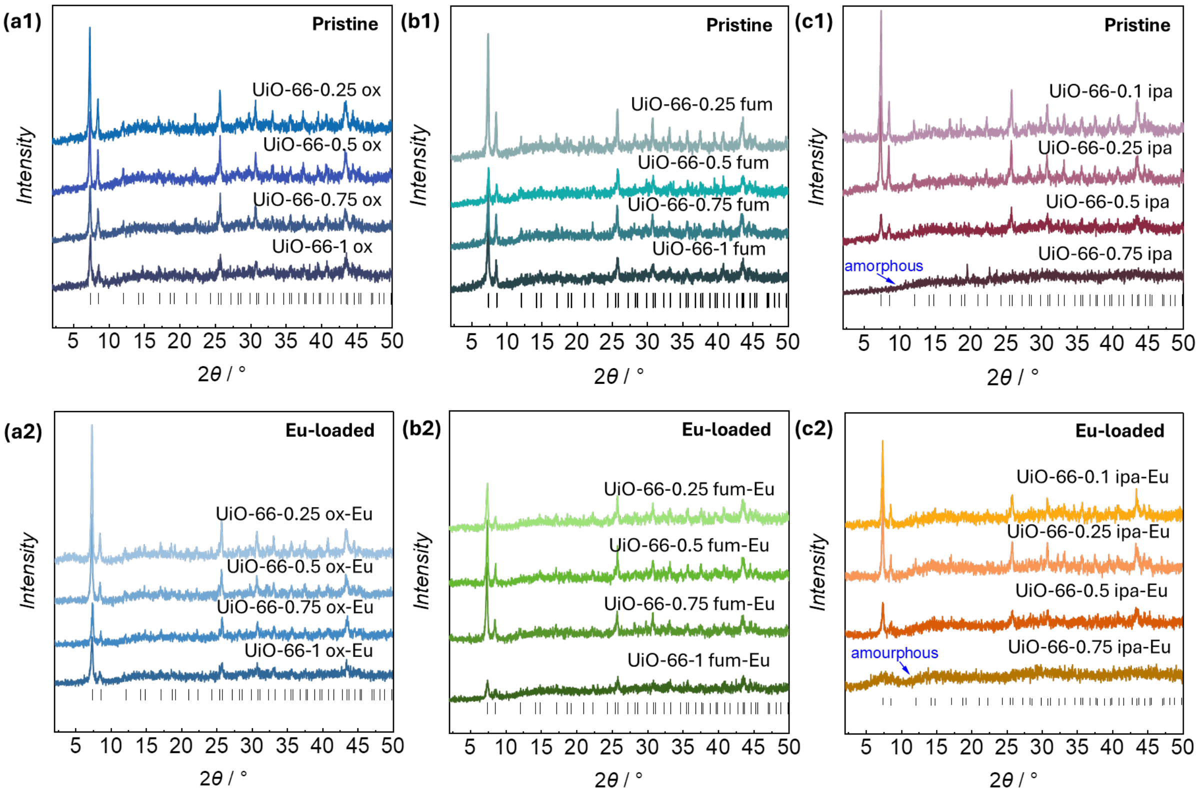

Figure S1. Powder X-ray diffractograms of as-synthesized UiO-66 derivatives: **(a)** UiO-66-*x* ox, **(b)** UiO-66-*x* fum and **(c)** UiO-66-*x* ipa. For each series, samples synthesized with increasing amounts of auxiliary dicarboxylic acids are shown from bottom to top. All patterns are compared to the reference UiO-66 diffractogram simulated from CCDC 733458. The oxalic- and fumaric-acid-modified samples retain the characteristic Fm-3m UiO-66 diffraction pattern, whereas high-ipa compositions (x = 0.75) exhibit a broad, featureless background indicative of amorphization.

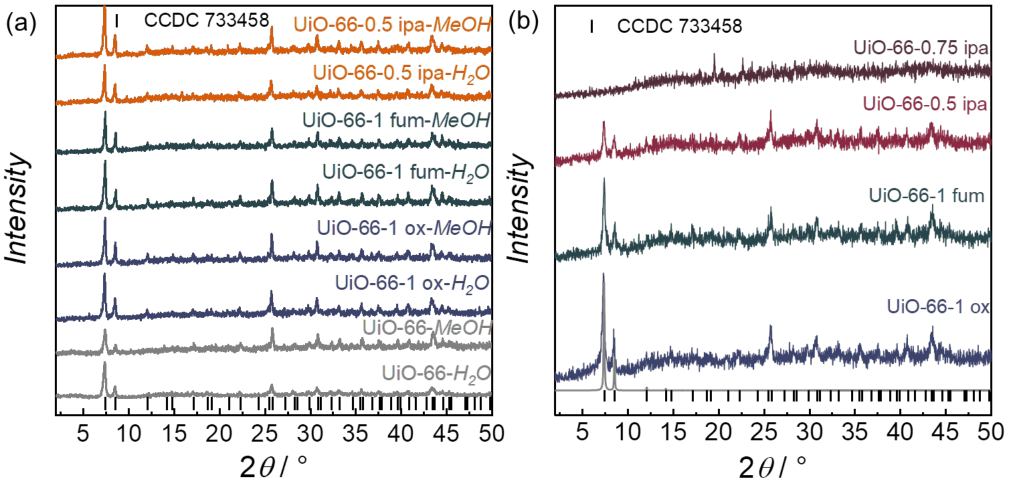

Figure S2. (a) PXRD-patterns of UiO-66-1 ox, UiO-66-1 fum and UiO-66-0.5 ipa after exposure to H_2O or MeOH under stirring for 12 h. For each case, the composition with the highest auxiliary-ligand content was selected as the most defect-rich representative. All samples retained crystallinity after solvent treatment. (b) Comparison of the experimental PXRD patterns of UiO-66-1 ox, UiO-66-1 fum, UiO-66-0.5 ipa and UiO-66-0.75 ipa with a simulated UiO-66 PXRD pattern (CCDC 733458). Reference Bragg positions of the UiO-66 phase are shown as black bars.

(a) UiO-66-x ox

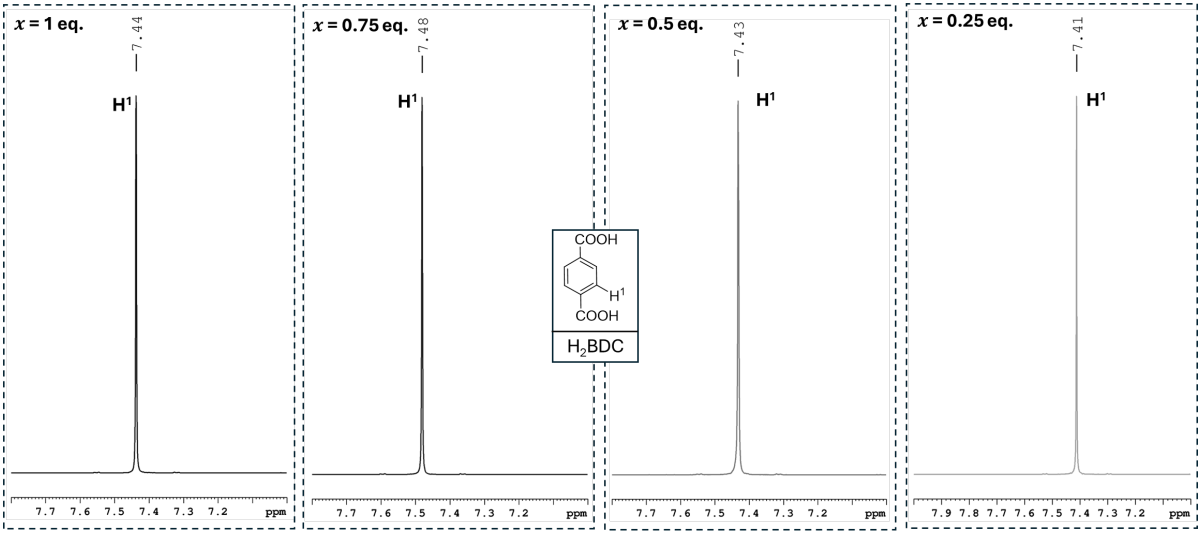

(b) UiO-66-x fum

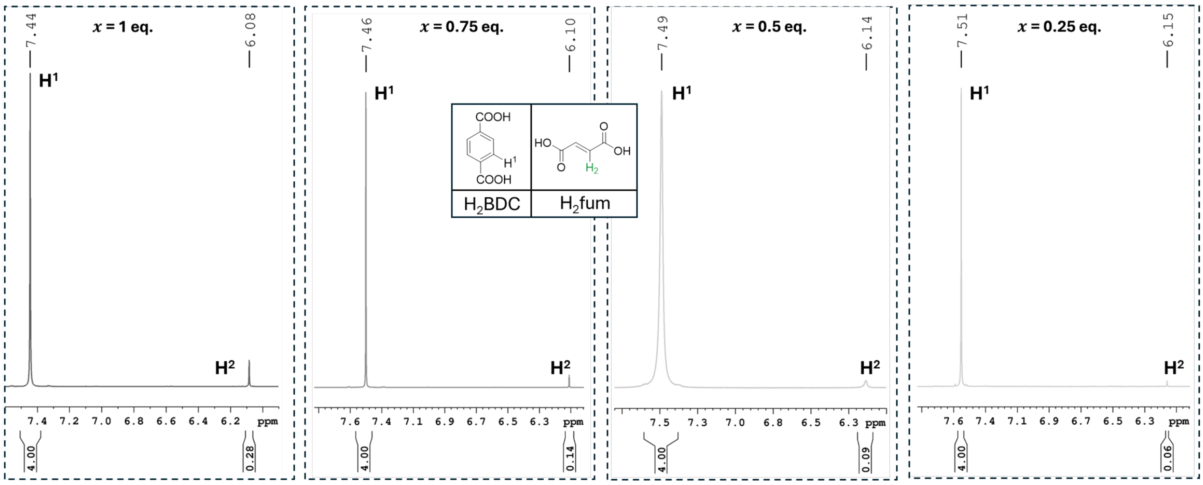

(c) UiO-66-x ipa

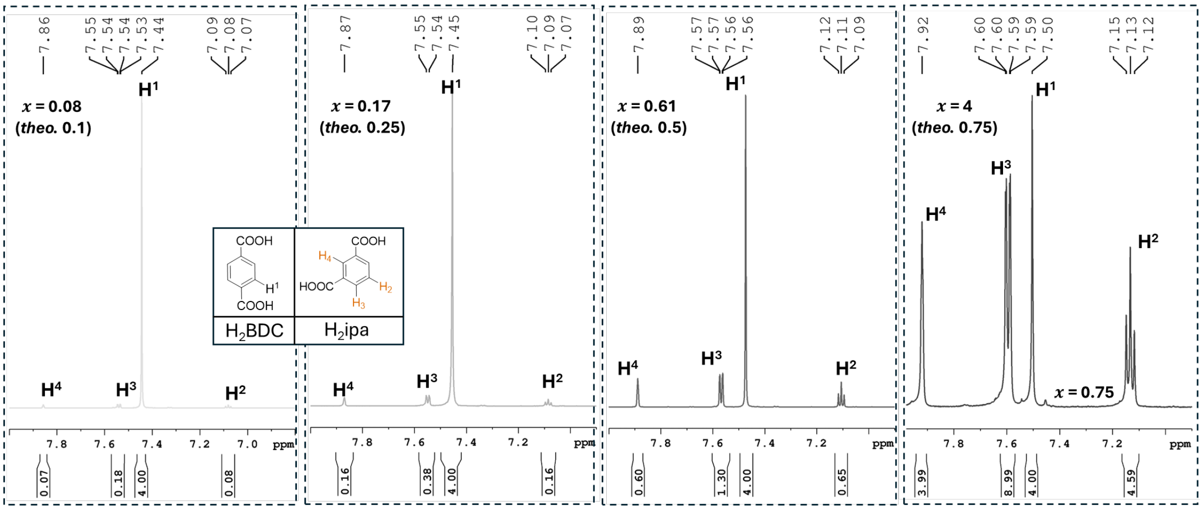

Figure S3 Solution ^{1}H-NMR-Spectra used to determine the relative incorporation of auxiliary dicarboxylic acids after digestion of the UiO-66-samples (using 1M K_3PO_4/DCl/D_2O): **(a)** UiO-66-*x* ox only proton signal from H_2BDC are detected and H_2ox is NMR-silent; **(b)** UiO-66 -*x* fum: proton resonances from both H_2BDC and fumaric acid enable quantification of the fumarate incorporation. **(c)** UiO-66-*x* ipa: aromatic proton signals from H_2BDC and

H_2ipa allow determination of the isophthalate fraction within the mixed-linker framework.

An example of the calculation of relative ratio between incorporated auxiliary dicarboxylic acid and terephthalic acid is shown here. In the NMR-spectrum of sample UiO-66-x ipa, one proton peak in H_2BDC and three distinct proton peaks in H_2ipa could be detected. The mean integral with respect to one proton in H_2BDC and H_2ipa should be:

$$\bar{I}_{H_2BDC} = \frac{1}{4}(I_{H^1}) \text{ and } \bar{I}_{H_2ipa} = \frac{1}{4}(I_{H^2} + I_{H^4} + 2I_{H^3})$$

The mean integral value could be regarded as normalized relative value of H_2BDC and H_2ipa. Thus, the relative ratio between H_2BDC and H_2ipa should be:

$$x = \frac{\bar{I}_{H_2ipa}}{\bar{I}_{H_2ipa} + \bar{I}_{H_2BDC}} = \frac{n_{H_2ipa}}{n_{H_2ipa} + n_{H_2BDC}}$$

(a) UiO-66-x fum-Eu

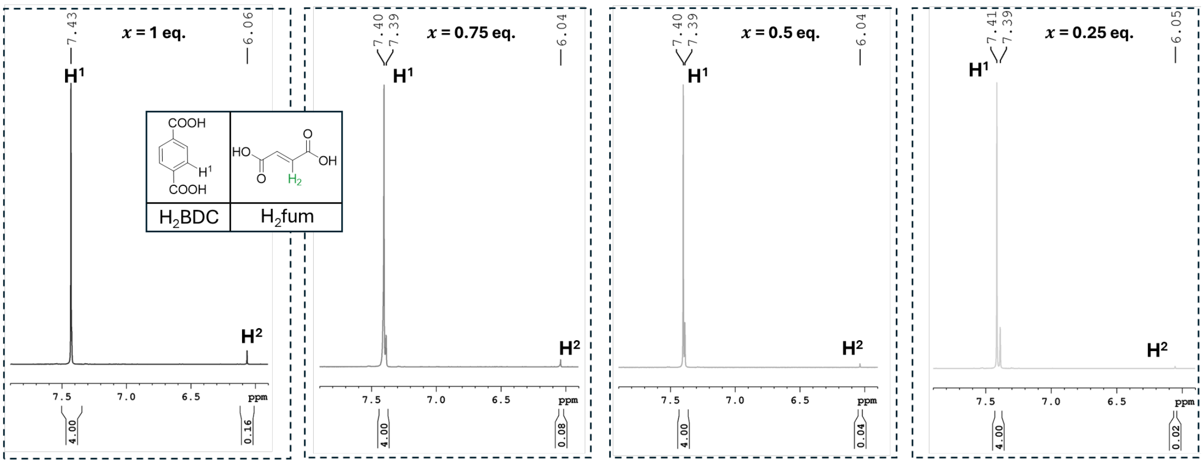

(b) UiO-66-x ipa-Eu

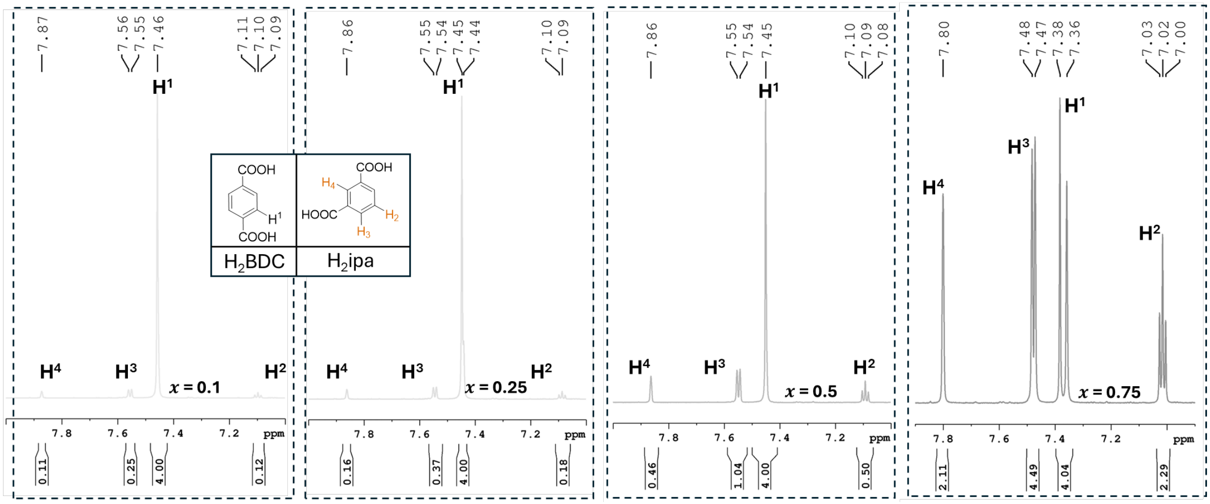

Figure S4 Solution ^{1}H-NMR-Spectra used to determine the relative incorporation of auxiliary dicarboxylic acids after digestion of the UiO-66-Eu-samples (using 1M K_3PO_4/DCl/D_2O): **(a)** UiO-66-*x* ox-Eu only proton signal from H_2BDC are detected and H_2ox is NMR-silent; **(b)** UiO-66 -*x* fum-Eu: proton resonances from both H_2BDC and fumaric acid enable quantification of the fumarate incorporation. **(c)** UiO-66-*x* ipa-Eu: aromatic proton signals from H_2BDC and H_2ipa allow determination of the isophthalate fraction within the mixed-linker framework.

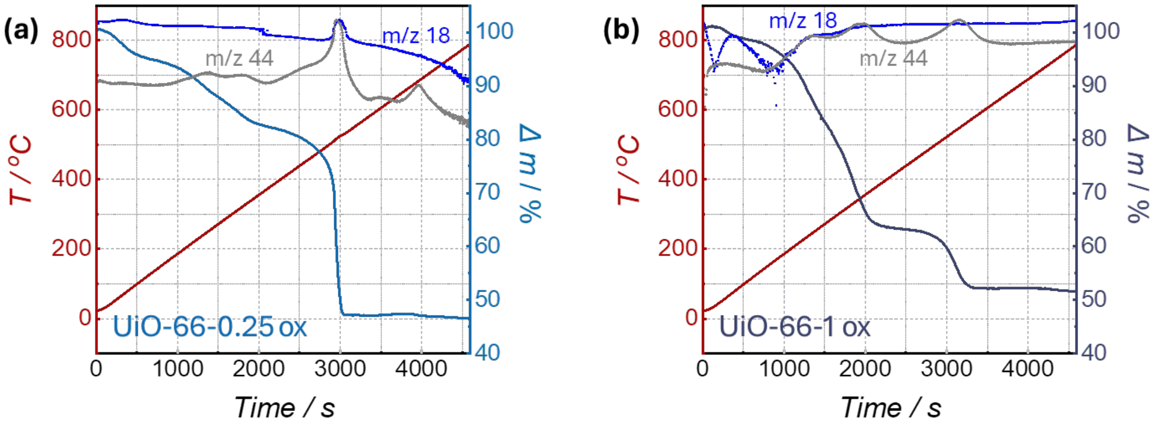

Figure S5 Thermogravimetric analysis coupled with mass-spectrometry (TGA-MS) of the **(a)** UiO-66-0.25 ox and **(b)** UiO-66-1 ox. Both samples exhibit characteristic multi-step decomposition profile of UiO-66, while the high-ox sample shows an additional significant mass-loss contribution between ca. 250-450 °C. The MS signals m/z=44 ($CO2^+$) and m/z=18 ($H2O^+$) indicates the release of decarboxylation- and dehydration-related species. The pronounced m/z 44 ($CO2^+$) signal in UiO-66-1 ox is consistent with the presence of extra non-BDC carboxylate species, supporting the incorporation of oxalate in the defect-modulated framework.

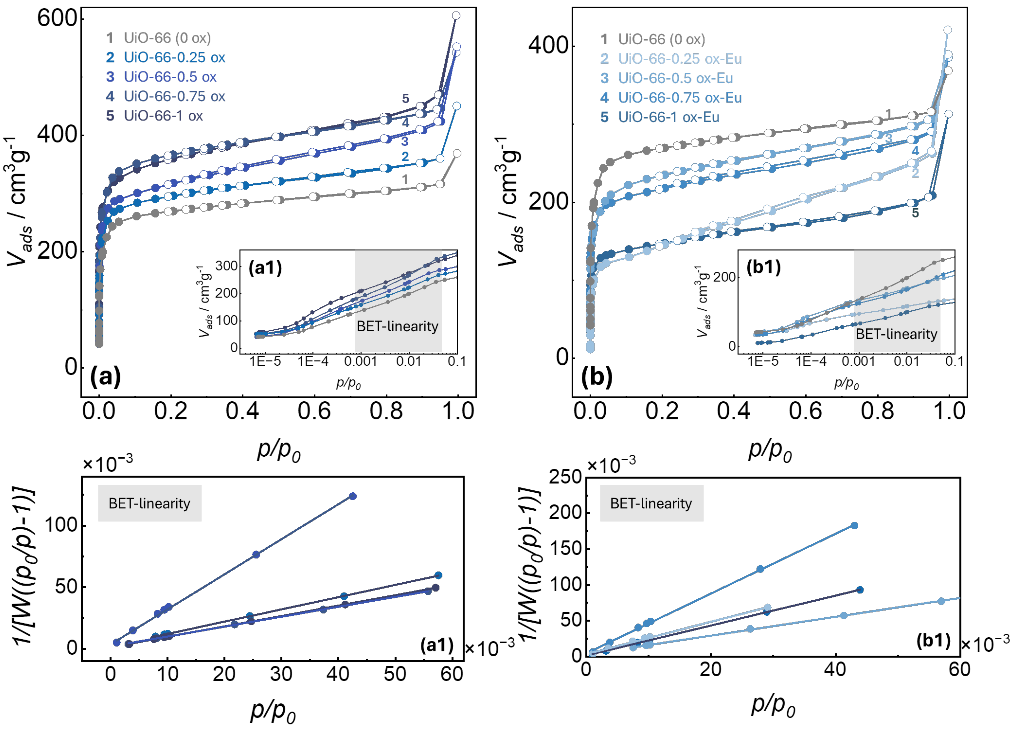

Figure S6 Nitrogen sorption isotherm of **(a)** UiO-66-*x* ox, **(b)** UiO-66-*x* fum and **(c)** UiO-66-*x* ipa and their sorption isotherm curves represented in semi-logarithmic axis as microporous materials with type I character.

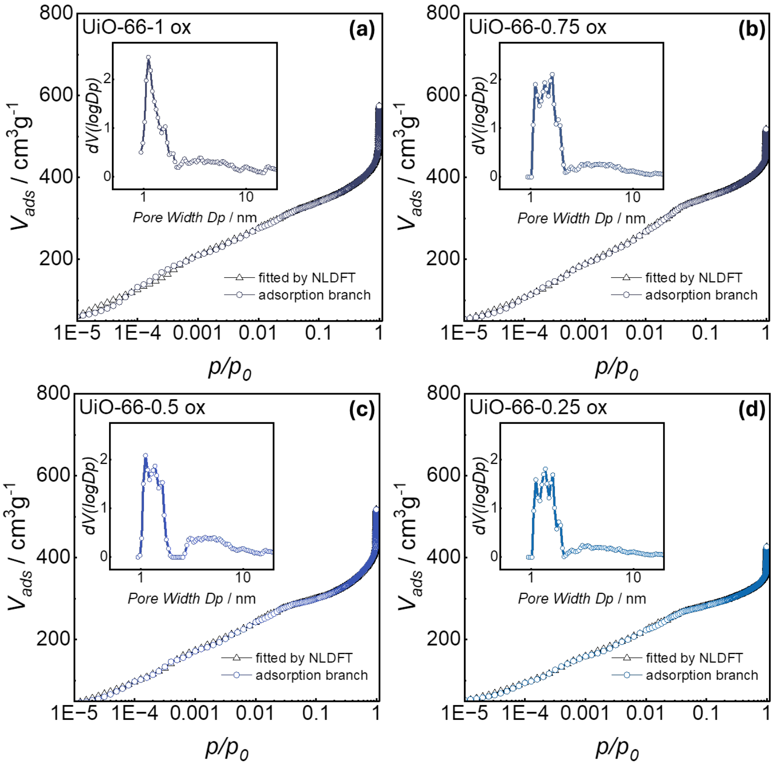

Figure S7 NLDFT-fitted nitrogen sorption data (triangle points) compared with measured data (circles points) in semi-logarithmic plot. The calculated pore width distribution is in good agreement with the theoretically calculated UiO-66 pore width distribution with/without defective region. A general broadening of pore width at about 1 nm could be observed, which is consistent with the work of M.J.Katz[1] and P.Chammingkwan[2] when considering defect formation.

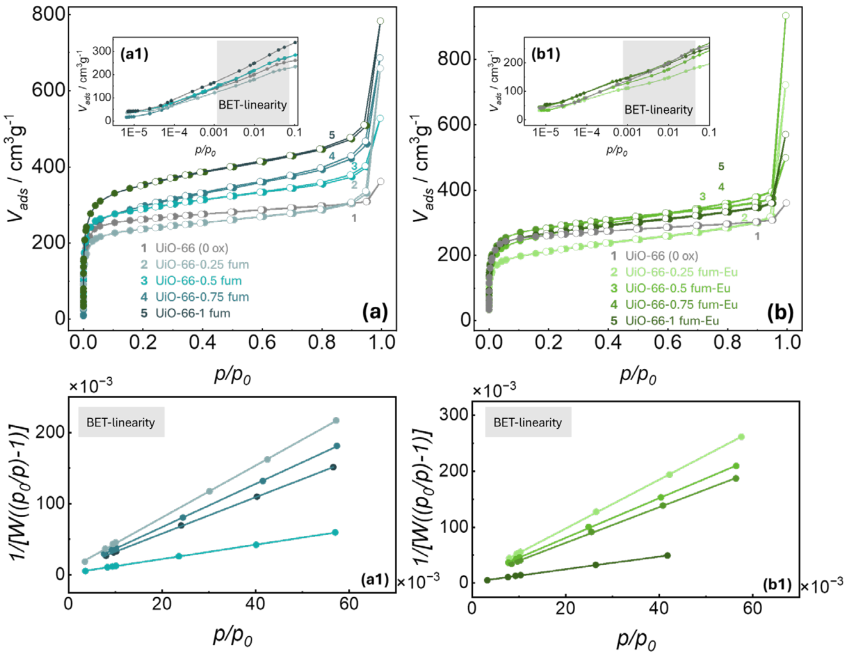

Figure S8 Nitrogen sorption isotherm of **(a)** UiO-66- *x* ox, **(b)** UiO-66- *x* fum and **(c)** UiO-66-*x* ipa and their sorption isotherm curves represented in semi-logarithmic axis as microporous materials with type I character.

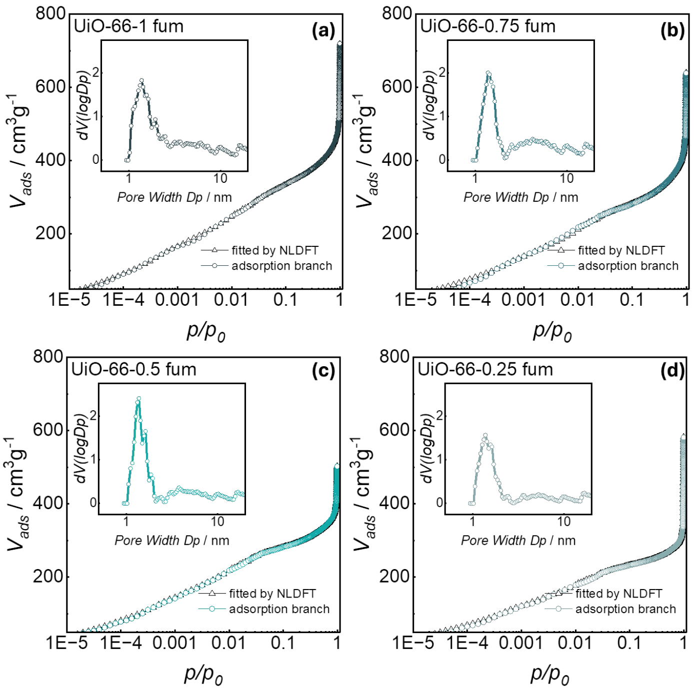

Figure S9 NLDFT-fitted nitrogen sorption data (triangle points) compared with measured data (circles points) in semi-logarithmic plot. The calculated pore width distribution is in good agreement with the theoretically calculated UiO-66 pore width distribution with/without defective region. A general broadening of pore width at about 1 nm could be observed, which is consistent with the work of M.J.Katz[1] and P.Chammingkwan[2] under consideration of defect.

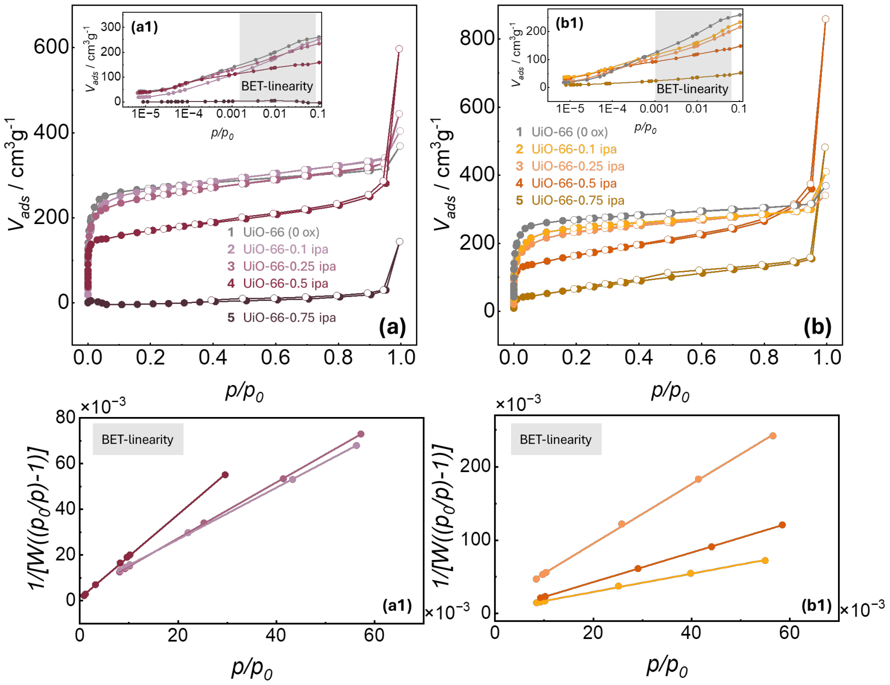

Figure S10 Nitrogen sorption isotherm of **(a)** UiO-66-*x* ox, **(b)** UiO-66-*x* fum and **(c)** UiO-66-*x* ipa and their sorption isotherm curves represented in semi-logarithmic axis as microporous materials with type I character.

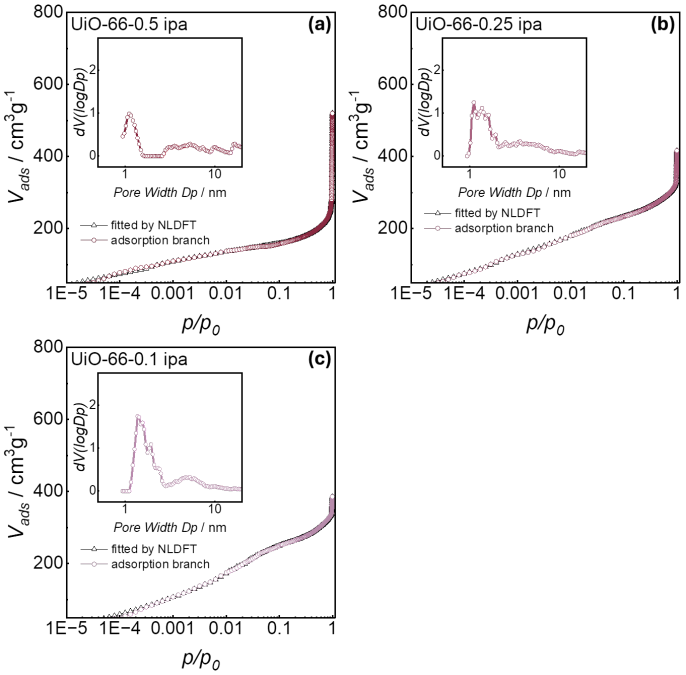

Figure S11 NLDFT-fitted nitrogen sorption data (triangle points) compared with measured data (circles points) in semi-logarithmic plot. The calculated pore width distribution is in good agreement with the theoretically calculated UiO-66 pore width distribution with/without defective region. A general broadening of pore width at about 1 nm could be observed, which is consistent with the work of M.J.Katz[1] and P.Chammingkwan[2] when considering defect formation.

Table S2. Experimental and NLDFT-fitted BET-surface area (**S_{BET}** and **$S_{BET,\ NLDFT}$** in m^{2}g^{-1}) and pore volume (**V_{pore}** in cm^{3}g^{-1}) of pristine samples and europium loaded samples after post-synthetic synthesis. The obtained surface area has no obvious linear tendence with increasing amount of fremd carboxylic acid. A general enlargement of surface area and pore volume could be observed with increasing amount of oxalic acid, fumaric acid, while after incorporation of isophthalic acid has opposite effect. After coordination with europium, a significant decrease of the surface area and pore volume decrease is notable.

(a) UiO-66-x ox

	UiO-66-HCl (0 eq)	**0.25eq**	***0.25eq-Eu***	**0.5eq**	***0.5eq-Eu***	**0.75eq**	***0.75eq-Eu***	**1eq**	***1eq-Eu***
S_{BET} / m^{2}g^{-1}	1246	1219	*704*	1468	*833*	1823	*1117*	1737	*653*
$S_{BET,NLDFT}$ / m^{2}g^{-1}	1175	1325	*748*	1321	*696*	1514	*965*	1566	*531*
V_{pore} / cm^{3}g^{-1} @p/p$_0$ 0.89	0.48	0.54	*0.31*	0.63	*0.43*	0.67	*0.46*	0.70	*0.38*

(b) UiO-66-HCl-x fum

	0.25eq	***0.25eq-Eu***	**0.5eq**	***0.5eq-Eu***	**0.75eq**	***0.75eq-Eu***	**1eq**	***1eq-Eu***
S_{BET} / m^{2}g^{-1}	1219	*795*	1460	*977*	1125	*1078*	1360	*1290*
$S_{BET,NLDFT}$ / m^{2}g^{-1}	1325	*619*	1219	*1044*	1154	*832*	1350	*1169*
V_{pore} / cm^{3}g^{-1} @p/p$_0$ 0.89	0.54	*0.46*	0.60	*0.58*	0.67	*0.56*	0.75	*0.54*

(c) UiO-66-*x* ipa

	0.1 ipa	0.1ipa-Eu	0.25 ipa	0.25ipa-Eu	0.5 ipa	0.5ipa-Eu	0.75 ipa	0.75ipa-Eu
S_{BET} / m^2g^{-1}	1281	1184	1179	865	801	736	nonporous	
$S_{BET,NLDFT}$ / m^2g^{-1}	949	944	1011	745	862	757		
V_{pore} / cm^3g^{-1} @p/p_0 0.89	0.52	0.46	0.49	0.46	0.39	0.49		

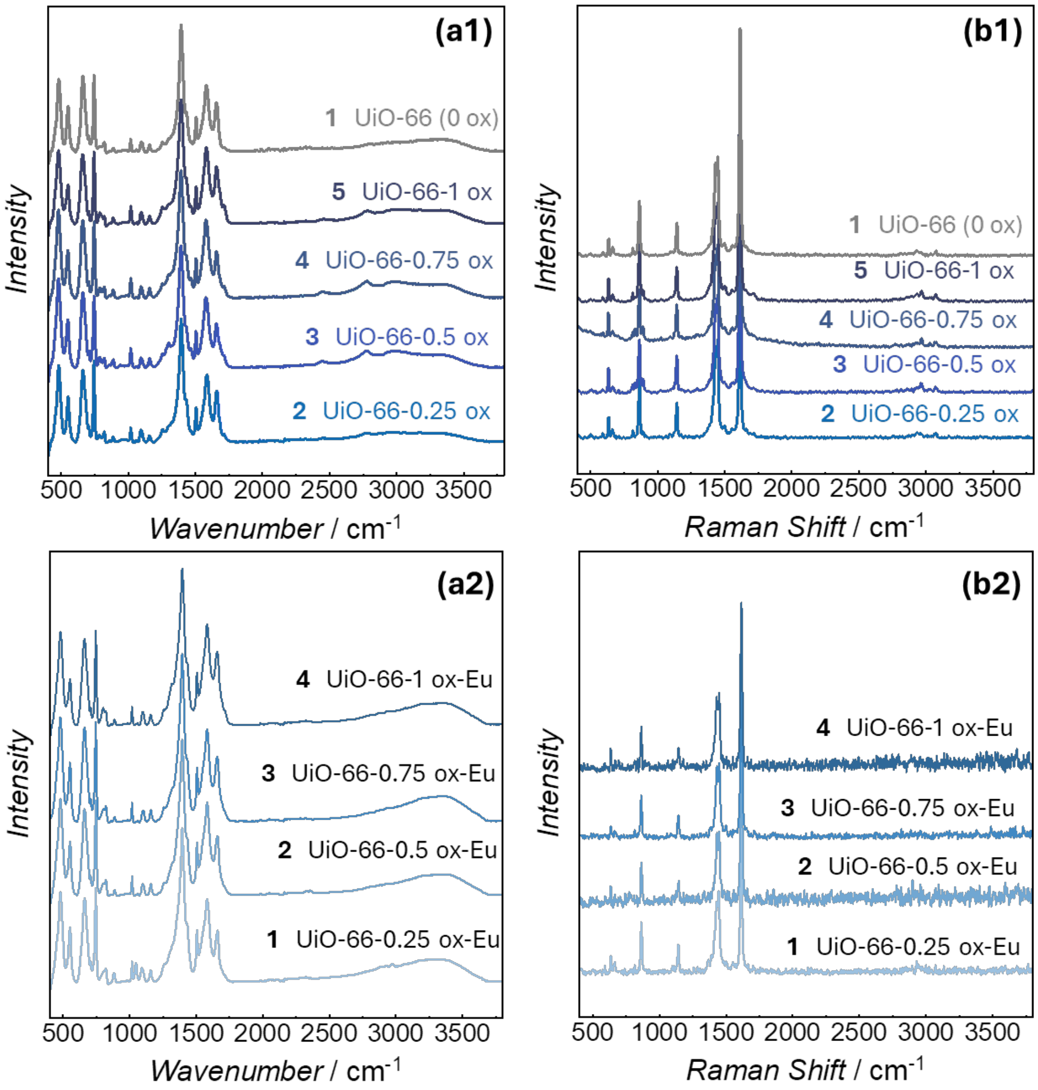

Figure S12 Full-range FTIR-ATR and Raman spectra of the UiO-66-*x* ox series before and after Eu^{3+} incorporation. Left panels: FITR-ATR spectra of UiO-66-x ox **(a1)** and UiO-66- x ox-Eu **(a2)**, showing characteristic Zr-O, C=O and O-C-O vibrational regions as well as changes associated with oxalate-modulated defects and Eu^{3+} coordination. Right panel: Corresponding Raman spectra for UiO-66-x ox **(b1)** and UiO-66-x ox-Eu **(b2)**, highlighting modifications in linker vibrations and metal-ligand interactions

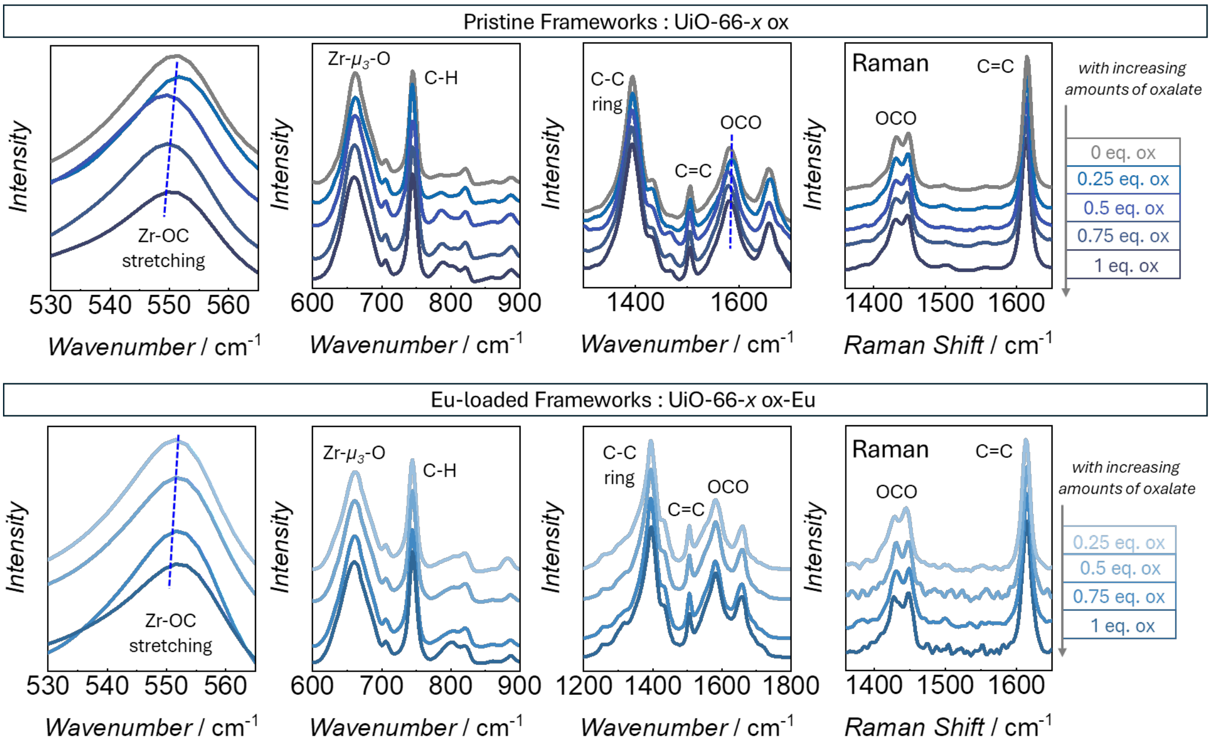

Figure S13 Selected FTIR-ATR and Raman spectral regions for UiO-66-*x* ox and UiO-66-*x* ox-Eu. For each series, spectra are shown from top to bottom in order of increasing modulator content (x = 0/0.25/0.5/0.75/1 eq). The FTIR-ATR panels highlight the evolution of the Zr-O-C stretching band (~550 cm^{-1}) and the O-C-O bending vibration (~680 cm^{-1}), both of which shift or vary in intensity upon incorporation of the auxiliary dicarboxylic acids. The Raman panels display the symmetric carboxylate stretching modes $v_{(COO-),sym.}$ (located between 1400-1500 cm^{-1}) in Raman spectra, revealing systematic spectral changes associated with the increasing defect concentration.

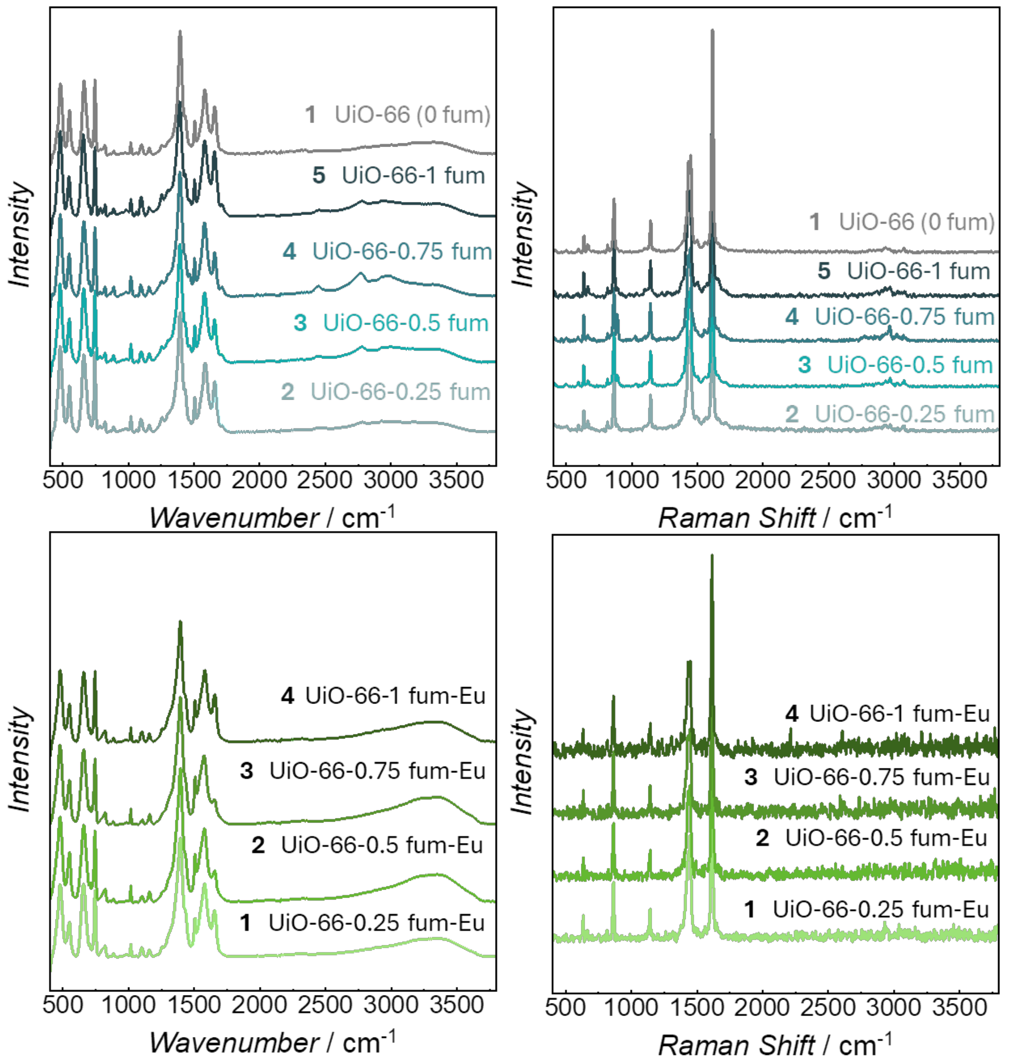

Figure S14 Full-range FTIR-ATR and Raman spectra of the UiO-66-*x* fum series before and after Eu^{3+} incorporation. Left panels: FITR-ATR spectra of UiO-66-x fum **(a1)** and UiO-66- x fum-Eu **(a2)**, showing characteristic Zr-O, C=O and O-C-O vibrational regions as well as changes associated with fumarate-modulated defects and Eu^{3+} coordination. Right panel: Corresponding Raman spectra for UiO-66-x fum **(b1)** and UiO-66-x fum-Eu **(b2)**, highlighting modifications in linker vibrations and metal-ligand interactions

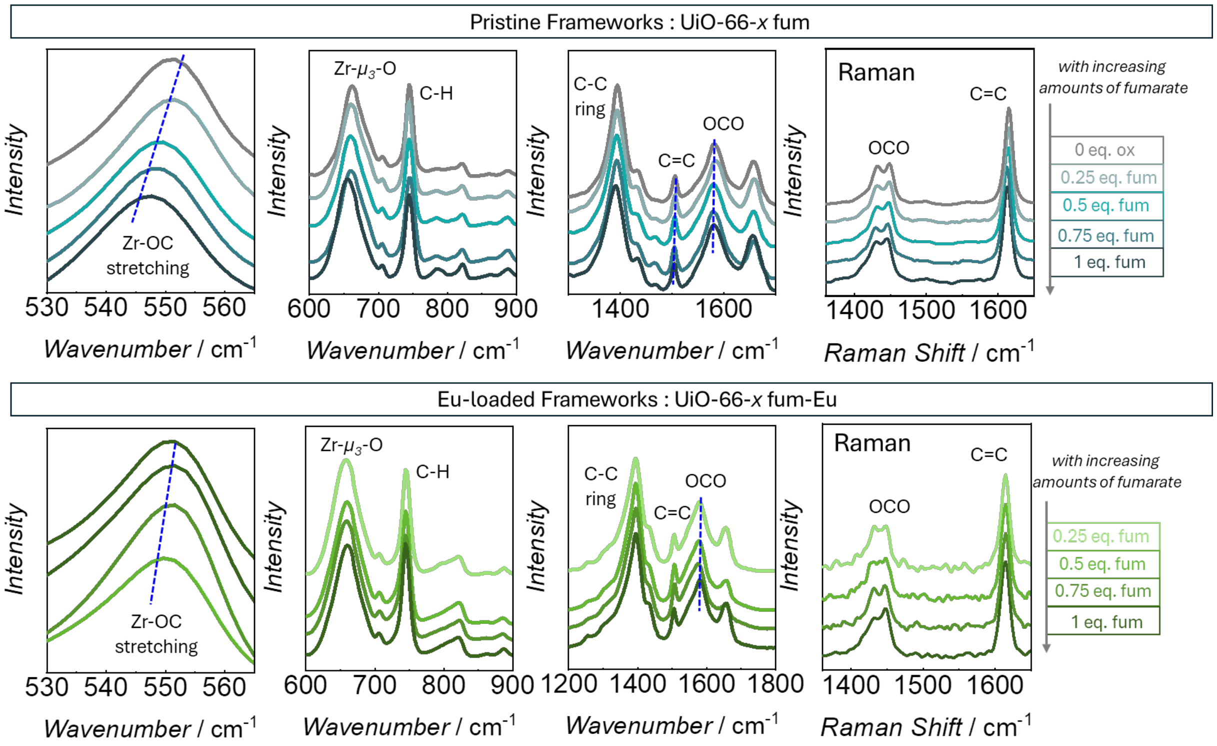

Figure S15 The truncated FTIR-ATR and Raman spectra of the samples UiO-66-*x* fum and UiO-66-*x* fum-Eu. In each spectrum, the grey curve is the reference material UiO-66 with pure BDC molecule. The curves are arranged from top to bottom in order of increasing modulator content. The comparison of the Zr-OC stretching (~550 cm^{-1}), OCO-bending (~1580 cm^{-1}) in FTIR-ATR spectra and the $\nu_{(COO-),sym.}$ (~1400-1500 cm^{-1}) in Raman spectra.

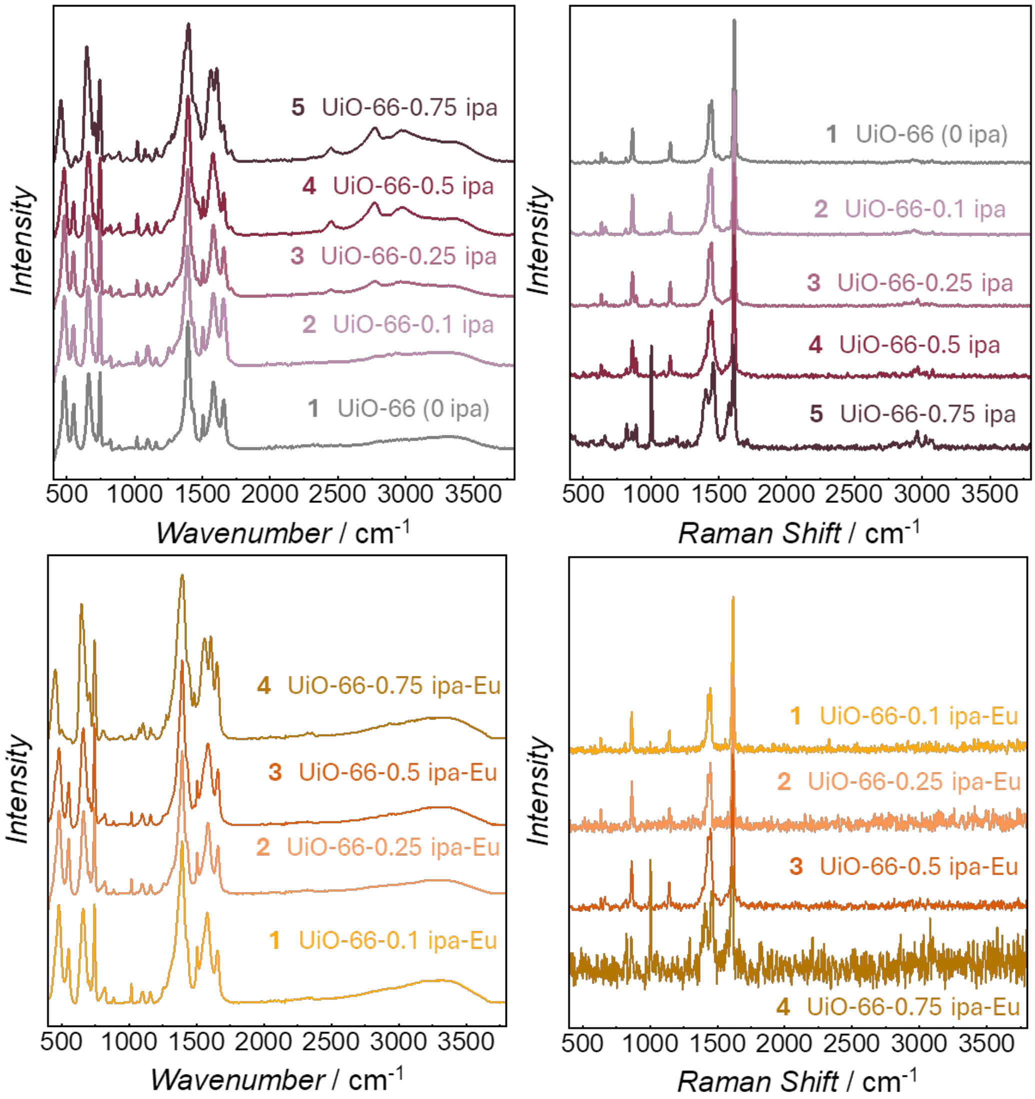

Figure S16 The FTIR-ATR spectra and Raman spectra of UiO-66-x ipa and UiO-66-x ipa-Eu in the whole region.

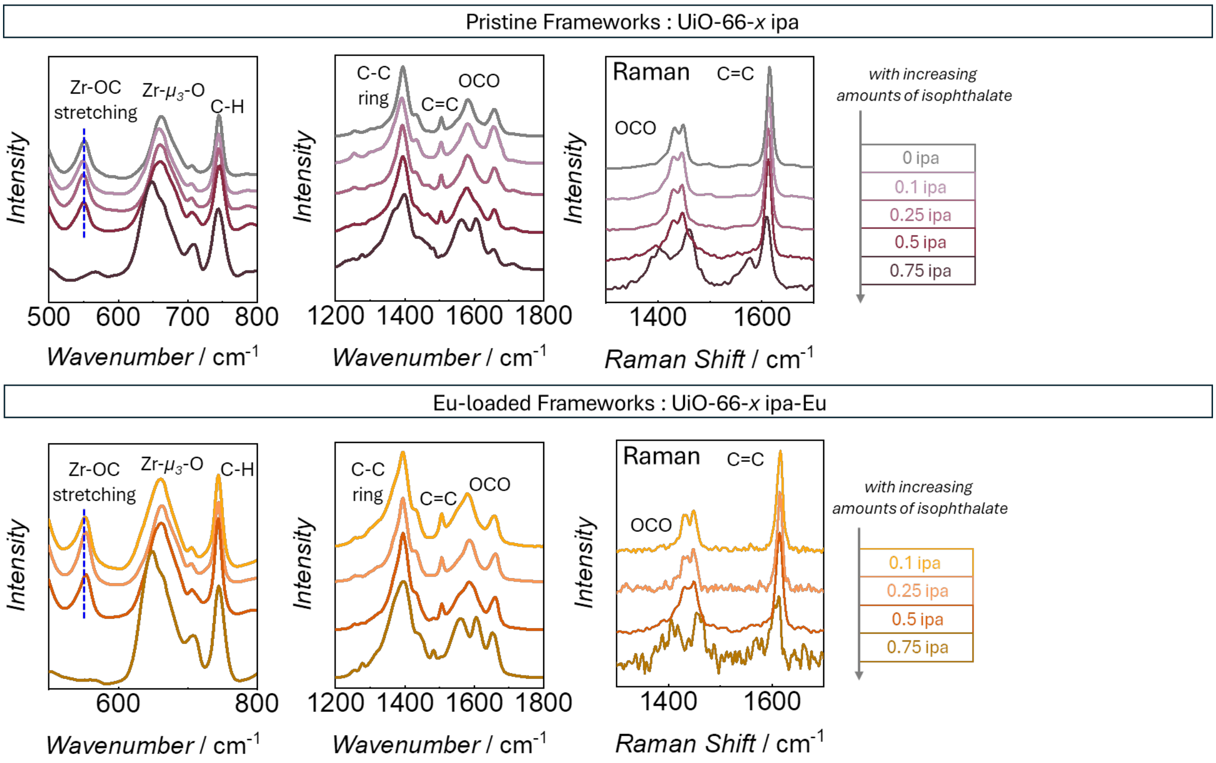

Figure S17 The truncated FTIR-ATR and Raman spectra of the samples UiO-66-*x* ipa and UiO-66-*x* ipa-Eu. In each spectrum, the grey curve is the reference material UiO-66 with pure BDC molecule. The curves are arranged from top to bottom in order to decrease the ipa content. The comparison of the Zr-OC stretching (~550 cm^{-1}), OCO-bending (~680 cm^{-1}) in FTIR-ATR spectra and the $v_{(COO-),sym.}$ (~1400-1500 cm^{-1}) in Raman spectra.

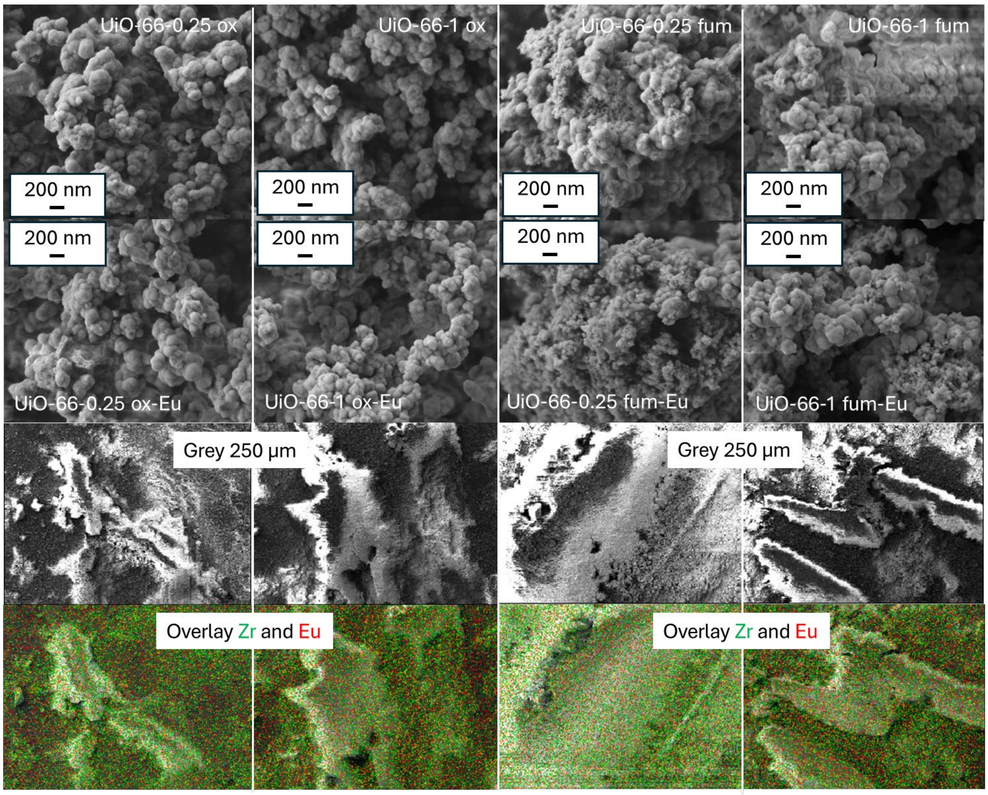

Figure S18 SEM micrographs of UiO-66-*x* ox, UiO-66-x fum and the europium loaded UiO-66-*x* ox-Eu and UiO-66-*x* fum-Eu. The EDX elemental maps confirm a homogeneous coexistence of Zr and Eu throughout the ~250 µm domain.

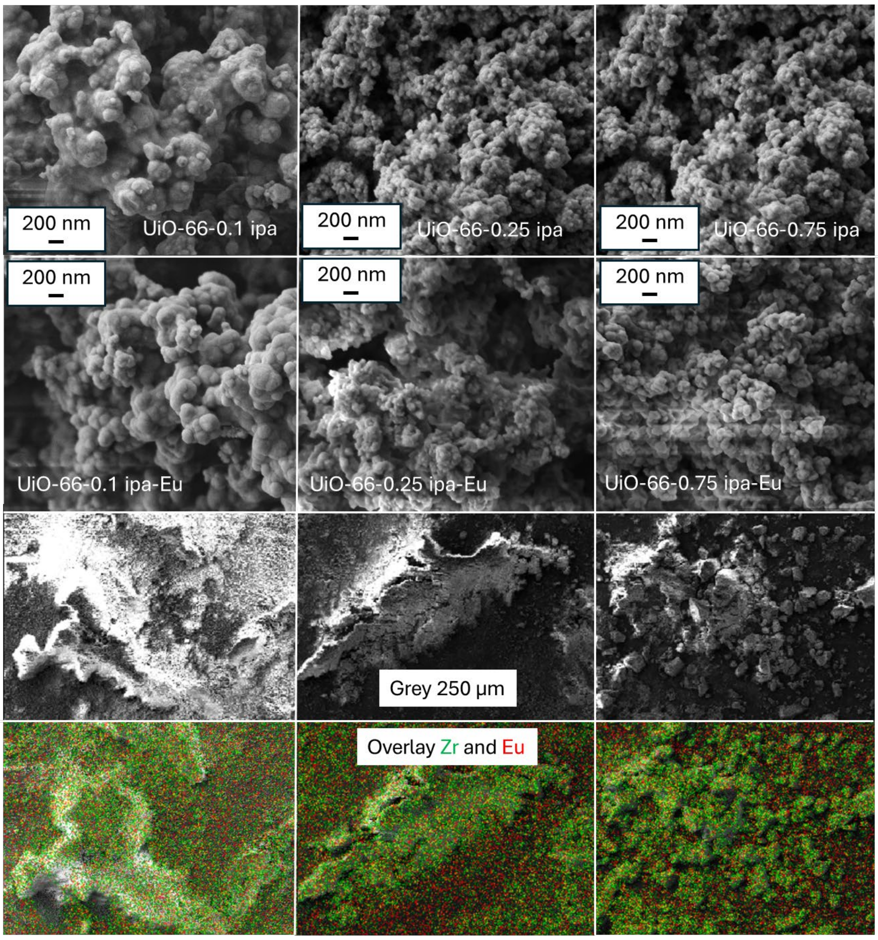

Figure S19 SEM micrographs of UiO-66-*x* ipa and the europium loaded UiO-66-*x* ipa-Eu. The EDX elemental maps confirm a homogeneous coexistence of Zr and Eu throughout the ~250 µm domain.

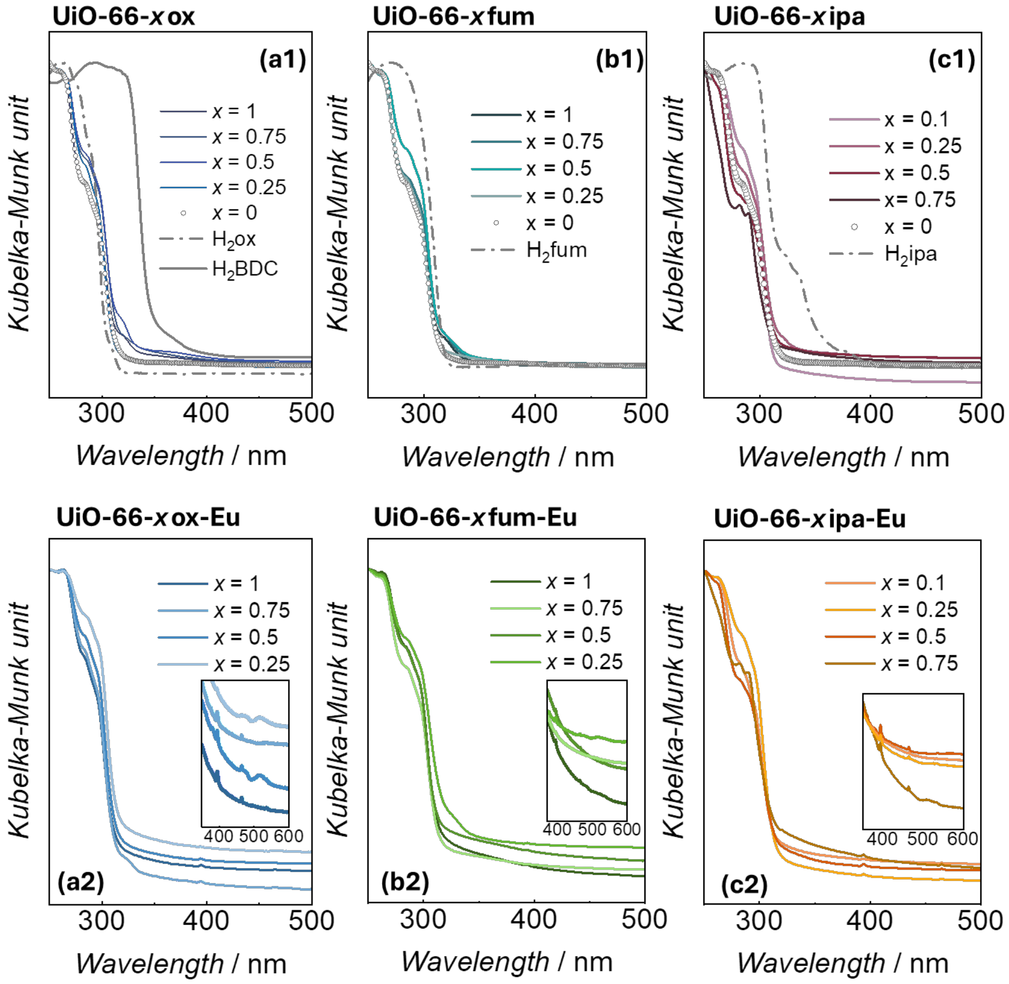

Figure S20 DRUV–Vis spectra of UiO-66-x frameworks incorporating different auxiliary dicarboxylic acids: oxalic (left), fumaric (middle), and isophthalic acid (right). **(a1)** Spectra of pristine UiO-66-x ox, **(b1)** Spectra of pristine UiO-66-x fum and **(c1)** UiO-66-x ipa. After europium loading, characteristic europium absorption transitions are observed. **(a2)** UiO-66-x ox-Eu, **(b2)** UiO-66-x fum-Eu and **(c2)** UiO-66-x ipa-Eu.

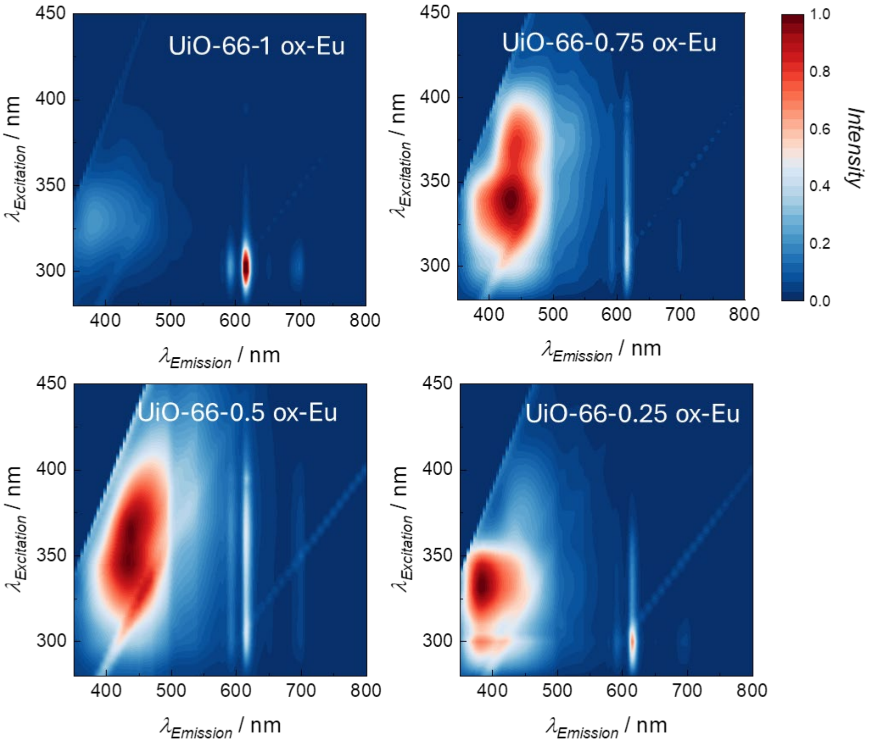

Figure S21 Three-dimensional excitation-emission spectra (EEMs) of the UiO-66-*x* ox-Eu series (x = 0.25, 0.5, 0.75, 1). All samples exhibit sharp Eu^{3+} $^5D_0 \rightarrow ^7F_J$ line emissions and broad linker-centered excitation bands.

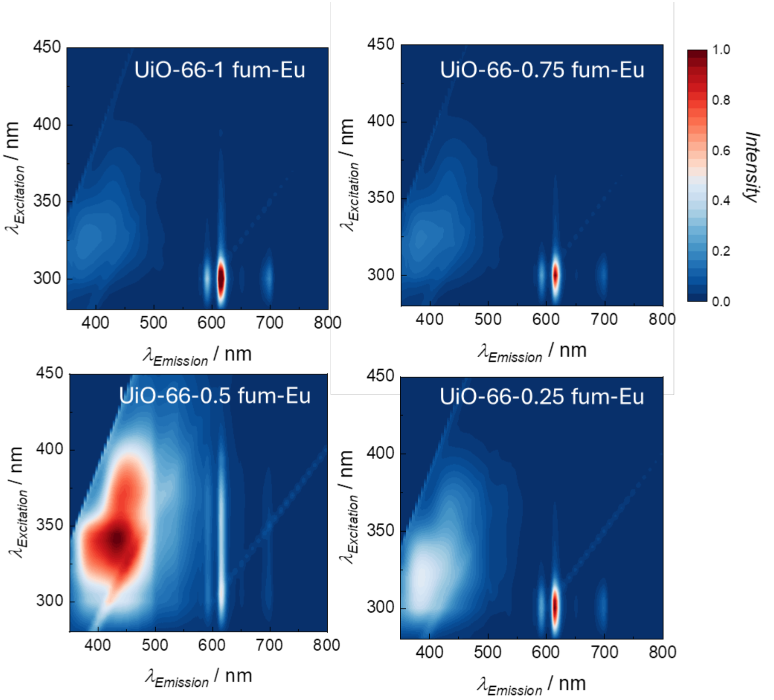

Figure S22. Three-dimensional excitation-emission spectra (EEMs) of the UiO-66-*x* fum-Eu series (x = 0.25, 0.5, 0.75, 1). All samples exhibit sharp Eu^{3+} $^5D_0 \rightarrow ^7F_J$ line emissions and broad linker-centered excitation bands.

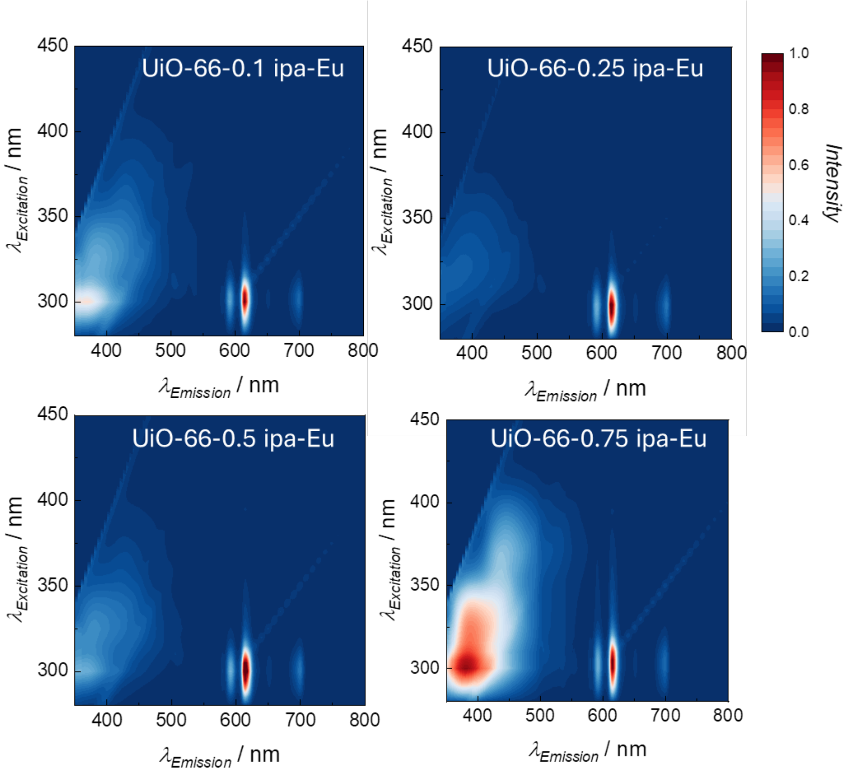

Figure S23. Three-dimensional excitation-emission spectra (EEMs) of the UiO-66-*x* ipa-Eu series (x = 0.25, 0.5, 0.75, 1). All samples exhibit sharp Eu^{3+} $^5D_0 \rightarrow {}^7F_J$ line emissions and broad linker-centered excitation bands.

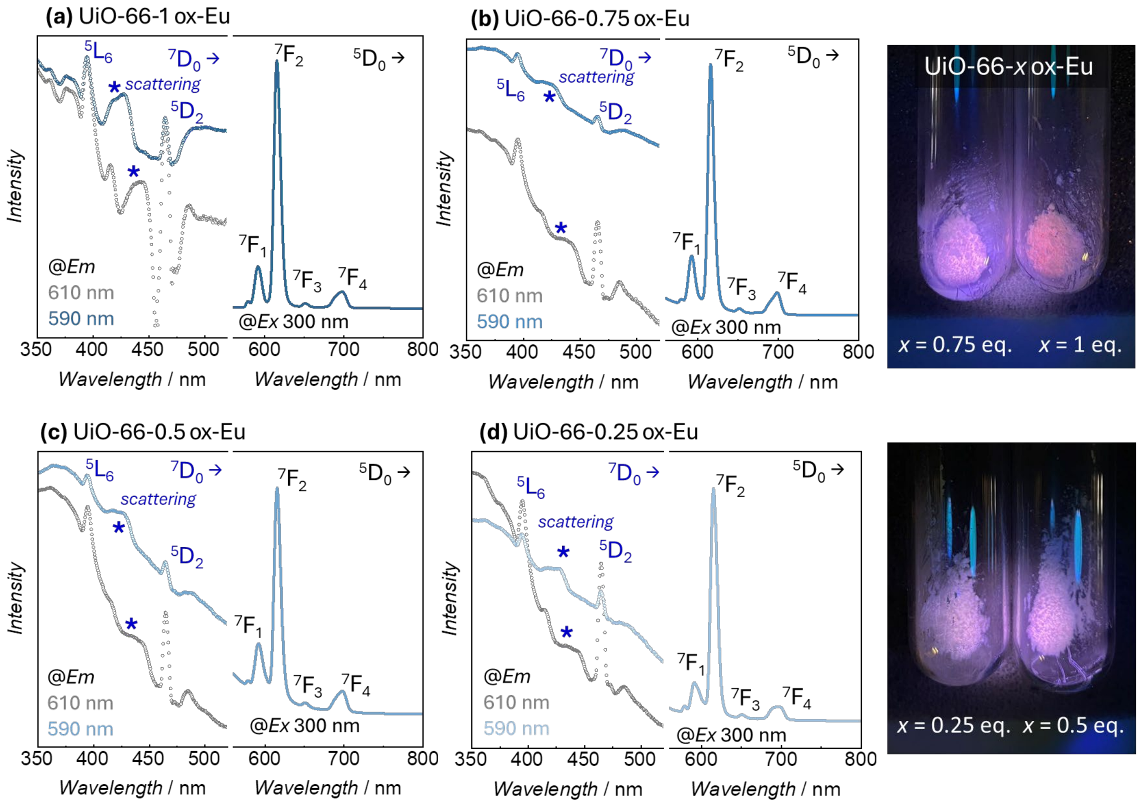

Figure S24 Excitation and emission spectrum of **(a)** UiO-66-1 ox-Eu, **(b)** UiO-66-0.75 ox-Eu, **(d)** UiO-66-0.5 ox-Eu and **(e)** UiO-66-0.25 ox-Eu. Upon illumination with UV-flash light under 375 nm, all samples show characteristic europium luminescence **(c,f)**.

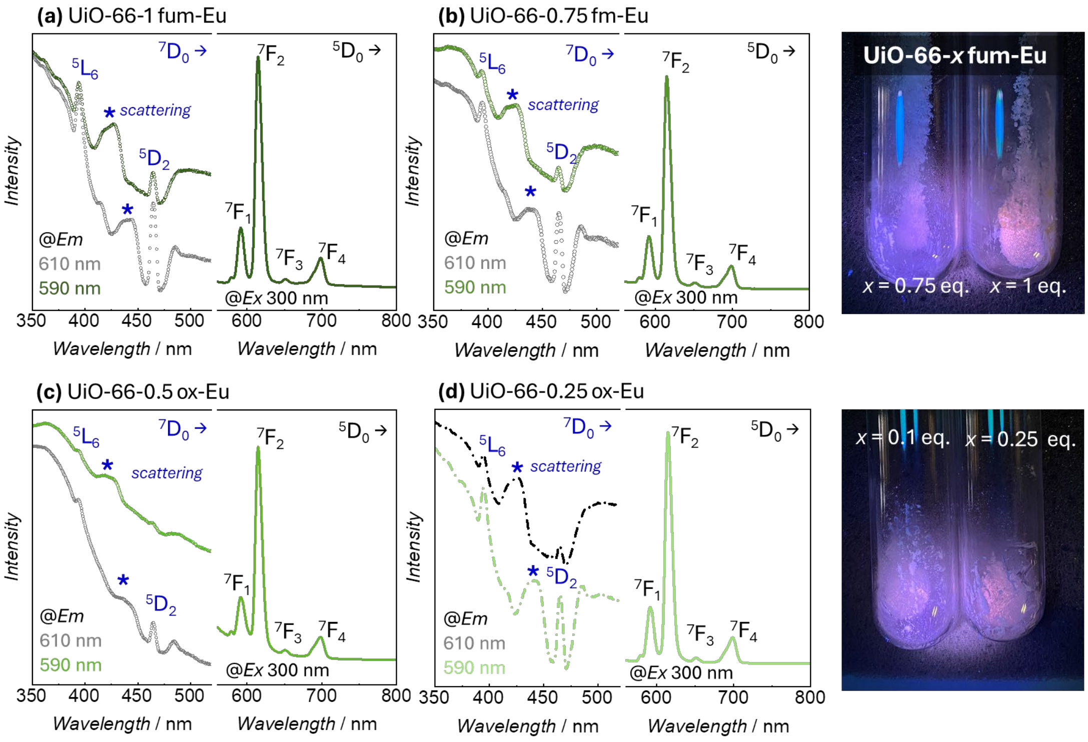

Figure S25 Excitation and emission spectrum of **(a)** UiO-66-1 fum-Eu, **(b)** UiO-66-0.75 fum-Eu, **(d)** UiO-66-0.5 fum-Eu and **(e)** UiO-66-0.25 fum-Eu. Upon illumination with UV-flash light under 375 nm, all samples show characteristic europium luminescence **(c,f)**.

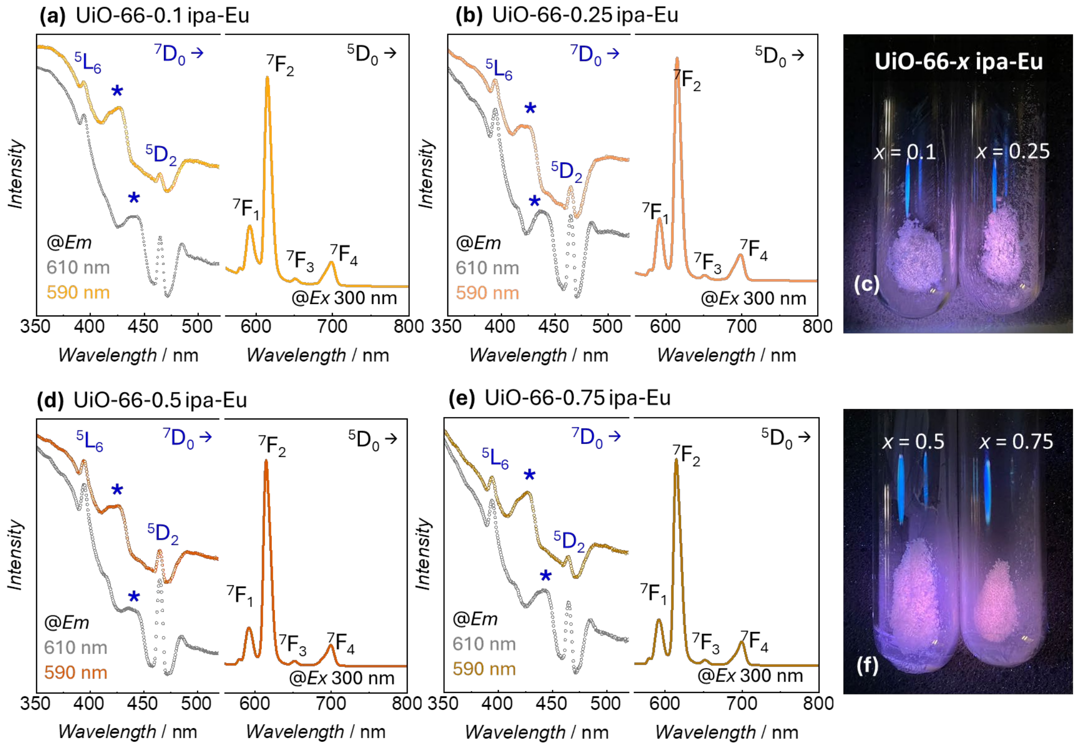

Figure S26 Excitation and emission spectrum of **(a)** UiO-66-0.1 ipa-Eu, **(b)** UiO-66-0.25 ipa-Eu, **(d)** UiO-66-0.5 ipa-Eu and **(e)** UiO-66-0.75 ipa-Eu. Upon illumination with UV-flash light under 375 nm, all samples show characteristic europium luminescence **(c,f)**.

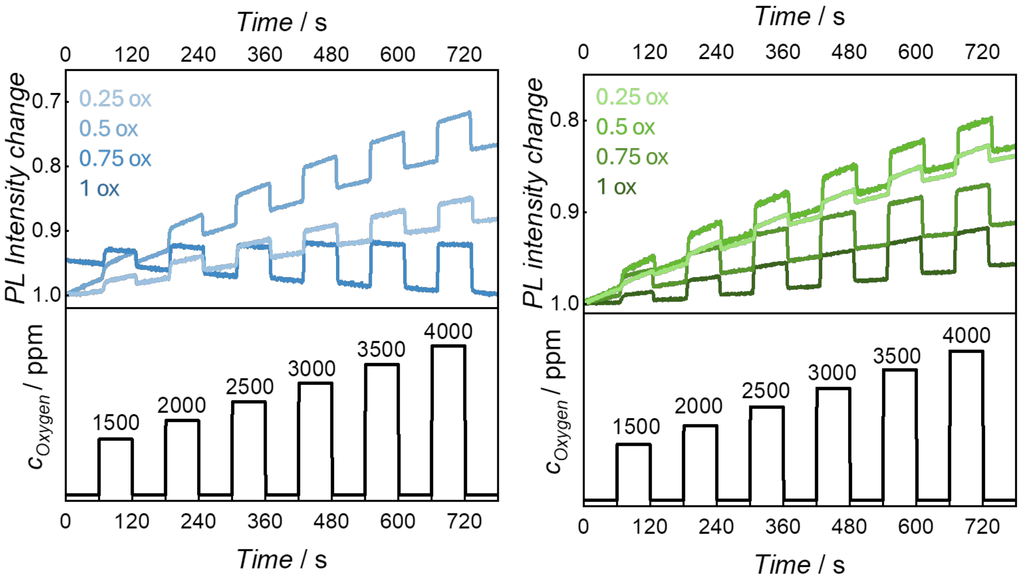

(a) UiO-66-*x* ox-Eu

(b) UiO-66-*x* fum-Eu

(c) UiO-66-*x* ipa-Eu

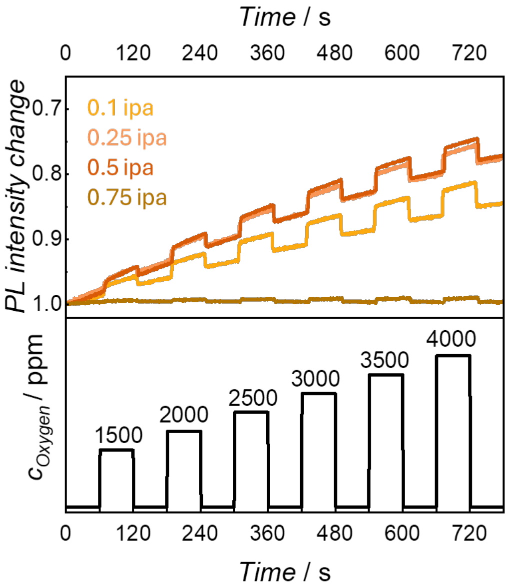

Figure S27 Test of reproducibility of oxygen-sensing response in reproduced Eu-loaded UiO-66 derivates. Time-dependent luminescence switching profiles ($\lambda_{ex.}$ = 300 nm, $\lambda_{em.}$ = 614 nm) of independently synthesized batches of **(a)** UiO-66-x ox-Eu, **(b)** UiO-66-x fum-Eu, and **(c)** UiO-66-x ipa-Eu, measured under alternating N_2/O_2 atmospheres. All compositions show highly reproducible and reversible intensity modulation upon oxygen exposure, confirming the robustness of the defect-assisted europium coordination environments. The amorphous/nonporous UiO-66-0.75 ipa-Eu shows negligible response, consistent with the loss of accessible porosity.

To evaluate the collisional Stern-Volmer behaviors from lifetime data, we calculated the effective dynamic Stern-Volmer constant. This allows direct comparison with the global intensity-based Stern-Volmer constant obtained from fitting across the entire measured oxygen-concentration range (as reported in the main text) and provides additional insight into the underlying quenching mechanism. The lifetime-correlated dynamic Stern-Volmer constant is obtained from:

$$R = \frac{\tau_{Nitrogen}}{\tau_{Atmosphere}} = 1 + K_{SV.dyn.} \cdot p_{O_2} \tag{1}$$

Therefore, the dynamic Stern-Volmer constant under atmosphere (20.5 vol.-%, 0.205 bar O_2) is calculated as:

$$K_{SV.dyn.} = \frac{R-1}{p_{O_2}} = \frac{R-1}{0.205} \tag{2}$$

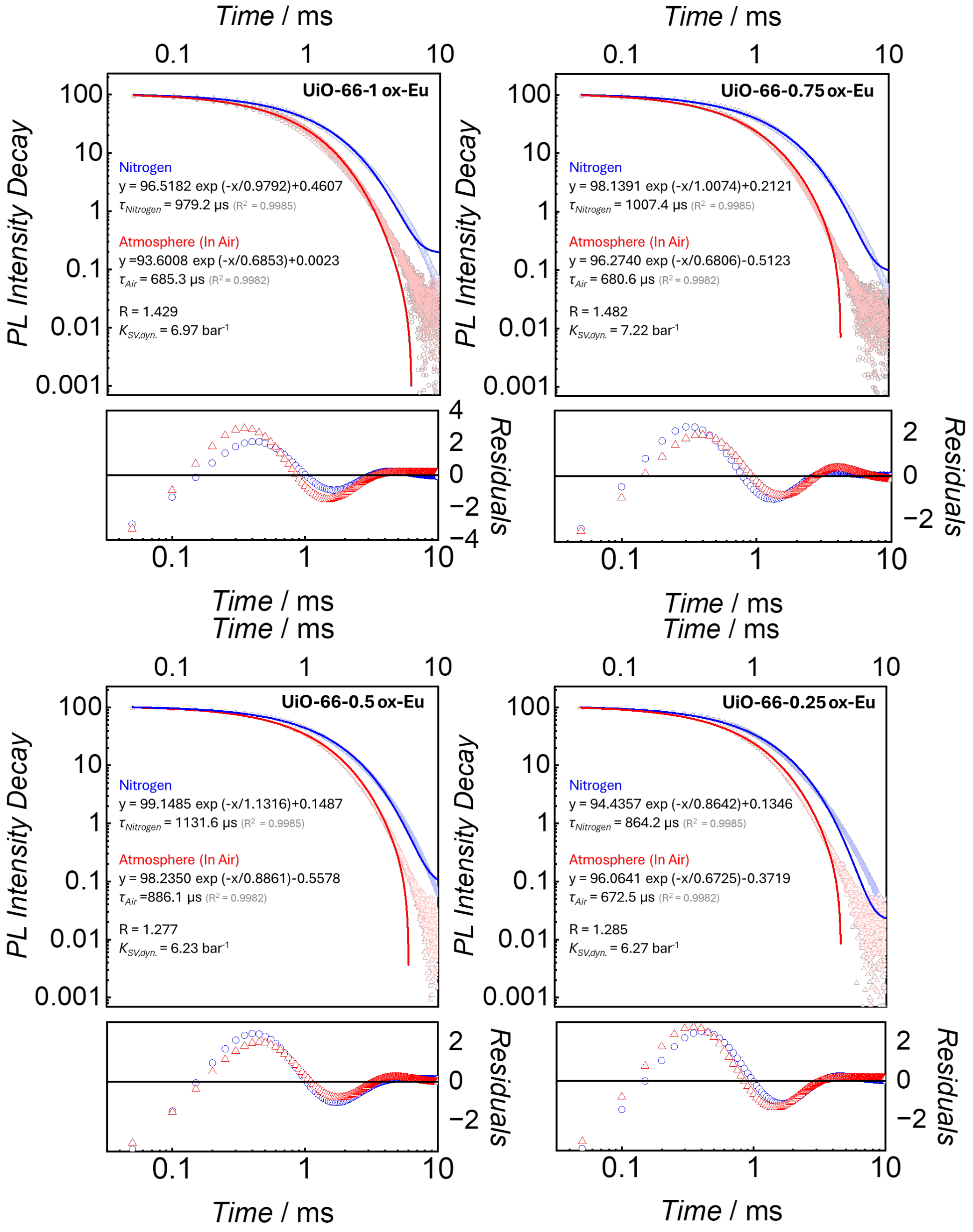

Figure S28. Time-resolved photoluminescence decay (chopping-modes, phase-modulated) of Eu-functionalized UiO-66 derivatives UiO-66-*x* ox-Eu measured under nitrogen (blue) and ambient atmosphere (~20.5 vol.% O_2, red).

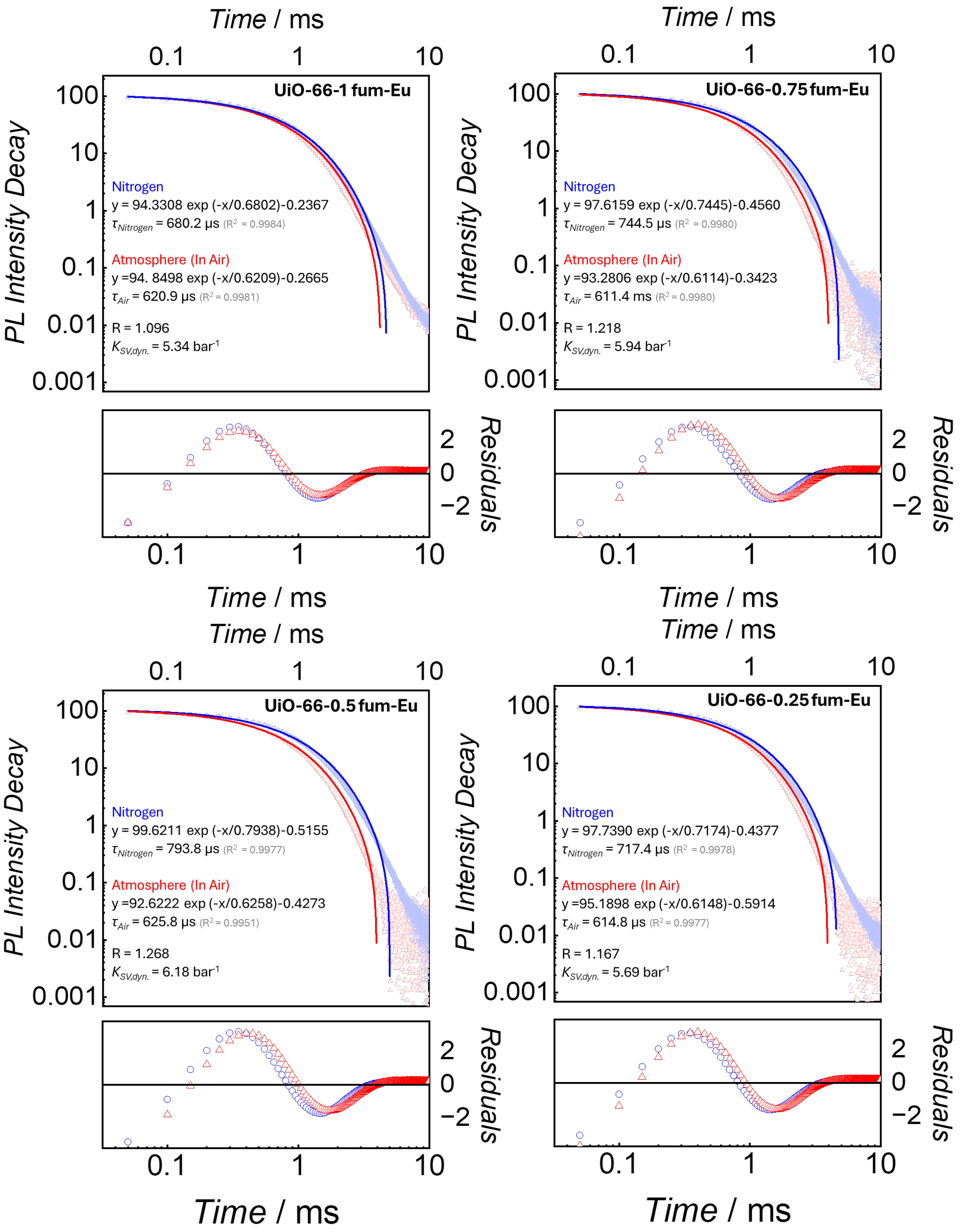

Figure S29. Time-resolved photoluminescence decay (chopping-modes, phase-modulated) of Eu-functionalized UiO-66 derivatives UiO-66-*x* fum-Eu measured under nitrogen (blue) and ambient atmosphere (~20.5 vol.% O_2, red).

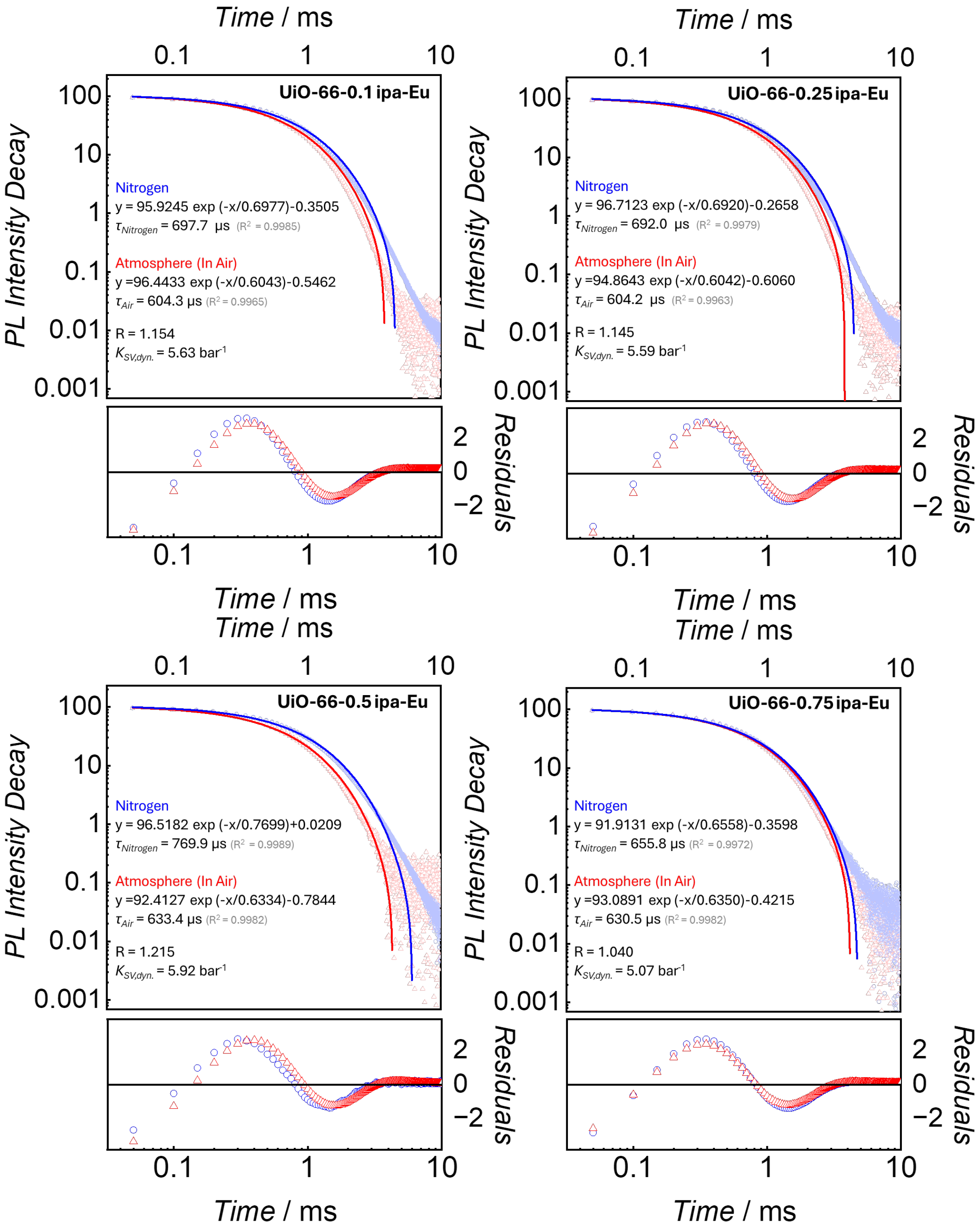

Figure S30. Time-resolved photoluminescence decay (chopping-modes, phase-modulated) of Eu-functionalized UiO-66 derivatives UiO-66-*x* ipa-Eu measured under nitrogen (blue) and ambient atmosphere (~20.5 vol.% O_2, red).

Table.S3. Survey of literature on O_2 sensing by lanthanide-based metal-organic frameworks (MOFs) or coordination polymers (CPs).

luminophore	K_{SV}* (bar^{-1})	$t_{response}$* (seconds)	$t_{recovery}$* (seconds)	refs.
df-UiO-66-Eu	**8.72-31.06**	***10***	***10***	**This work**
MOF-76(Eu/Y)	10.85	4.5	4.75	*Z.Zhao et al.*[3]
MCF-53(Tb/Eu_x)	0.85-2.99	n.r.	n.r.	J. Ye *et al.*[4]
Eu-NDC	13.3	10	70	T. Xia *et al.*[5]
SUMOF- 6(Eu)/O-PP	6.73	10	60	X. Xu *et al.*[6]
Tb(lll)@CPM-5(In)	0.78	60	90	Z. Dou *et al.*[7]
Tb(lll)@MIL-100(ln)	7.59	6	53	
Yb (lll)@bio-MOF-1	n.r.	n.r.	n.r.	J. An *et al.* [8]
Tb(lll)@bio-MOF- 1				
Eu-complex@bio-MOF-1	1.4-5.8	12-18	19	X. Qiao *et al.* [9]
Pyrene@ZIF-8(MAF-4)	3.43-6.09	n.r.	n.r.	J. Ye *et al.* [10]
Pt @ZIF-8	n.r.	n.r.	n.r.	T. Knedel *et al.*[11]
Pt@MOF-5				
MAF-2	356-213	n.r.	n.r.	S. Liu *et al.*[12]
lr-Zn-MOF	n.r.	n.r.	n.r.	Z.Xie *et al.*[13]
lr-Zn/Ni/Co/Cd-MOF	0.83-2.82	30-110	70-240	M.Ho *et al.* [14]
lr-UiO-67	78.6-89.43	n.r.	n.r.	S. Barrett *et al.*[15]
Ru-UiO-67	227.5			
Pt-UiO-type	13	n.r.	n.r.	R. Xu *et al.*[16]
MAF-X11	27	n.r.	n.r.	R. Lin *et al.*[17]
Ru(ll)$_x$@MAF-34	8.5-25	n.r.	n.r.	X. Qi *et al.*[18]
PCN-224	0.25	n.r.	n.r.	T. Burger *et al.*[19] J.Yang *et al.*[20]
PCN-224-Pt(II)	73			
PCN-224-Pd(II)	2610			
Ag_{12}bpy	n.r.	1 s	n.r.	X. Dong *et al.*[21]
Ag_{12}bpy-NH2	2.25×10^5	0.3 s	n.r.	

* n.r. = not reported

References

[1] M. J. Katz, Z. J. Brown, Y. J. Colón, P. W. Siu, K. A. Scheidt, R. Q. Snurr, J. T. Hupp, O. K. Farha, “A facile synthesis of UiO-66, UiO-67 and their derivatives” *Chem. Commun.* **2013**, *49*, 9449.

[2] P. Chammingkwan, G. Y. Shangkum, L. T. T. Mai, P. Mohan, A. Thakur, T. Wada, T. Taniike, “Modulator-free approach towards missing-cluster defect formation in Zr-based UiO-66” *RSC Adv.* **2020**, *10*, 28180–28185.

[3] Z. Zhao, C. Weinberger, J. Steube, M. Bauer, M. Brehm, M. Tiemann, “Fast-Responding O_2 Gas Sensor Based on Luminescent Europium Metal-Organic Frameworks (MOF-76)” *Adv Funct Materials* **2025**, e11190.

[4] J.-W. Ye, J.-M. Lin, Z.-W. Mo, C.-T. He, H.-L. Zhou, J.-P. Zhang, X.-M. Chen, “Mixed-Lanthanide Porous Coordination Polymers Showing Range-Tunable Ratiometric Luminescence for O_2 Sensing” *Inorg. Chem.* **2017**, *56*, 4238–4243.

[5] T. Xia, L. Jiang, J. Zhang, Y. Wan, Y. Yang, J. Gan, Y. Cui, Z. Yang, G. Qian, “A fluorometric metal-organic framework oxygen sensor: from sensitive powder to portable optical fiber device” *Microporous and*

Mesoporous Materials **2020**, *305*, 110396.

[6] X.-Y. Xu, B. Yan, “Nanoscale LnMOF-functionalized nonwoven fibers protected by a polydimethylsiloxane coating layer as a highly sensitive ratiometric oxygen sensor” *J. Mater. Chem. C* **2016**, *4*, 8514–8521.

[7] Z. Dou, J. Yu, Y. Cui, Y. Yang, Z. Wang, D. Yang, G. Qian, “Luminescent Metal–Organic Framework Films As Highly Sensitive and Fast-Response Oxygen Sensors” *J. Am. Chem. Soc.* **2014**, *136*, 5527–5530.

[8] J. An, C. M. Shade, D. A. Chengelis-Czegan, S. Petoud, N. L. Rosi, “Zinc-Adeninate Metal−Organic Framework for Aqueous Encapsulation and Sensitization of Near-infrared and Visible Emitting Lanthanide Cations” *J. Am. Chem. Soc.* **2011**, *133*, 1220–1223.

[9] X. Qiao, Z. Ma, L. Si, W. Ding, G. Xu, “Doping metal-organic framework with a series of europium-antenna cations: Obviously improved spectral response for O2 gas via long-range energy roll-back procedure” *Sensors and Actuators B: Chemical* **2019**, *299*, 126978.

[10] J.-W. Ye, H.-L. Zhou, S.-Y. Liu, X.-N. Cheng, R.-B. Lin, X.-L. Qi, J.-P. Zhang, X.-M. Chen, “Encapsulating Pyrene in a Metal–Organic Zeolite for Optical Sensing of Molecular Oxygen” *Chem. Mater.* **2015**, *27*, 8255–8260.

[11] T.-O. Knedel, S. Buss, I. Maisuls, C. G. Daniliuc, C. Schlüsener, P. Brandt, O. Weingart, A. Vollrath, C. Janiak, C. A. Strassert, “Encapsulation of Phosphorescent Pt(II) Complexes in Zn-Based Metal–Organic Frameworks toward Oxygen-Sensing Porous Materials” *Inorg. Chem.* **2020**, *59*, 7252–7264.

[12] S. Liu, X. Qi, R. Lin, X. Cheng, P. Liao, J. Zhang, X. Chen, “Porous Cu(I) Triazolate Framework and Derived Hybrid Membrane with Exceptionally High Sensing Efficiency for Gaseous Oxygen” *Adv Funct Materials* **2014**, *24*, 5866–5872.

[13] Z. Xie, L. Ma, K. E. deKrafft, A. Jin, W. Lin, “Porous Phosphorescent Coordination Polymers for Oxygen Sensing” *J. Am. Chem. Soc.* **2010**, *132*, 922–923.

[14] M.-L. Ho, Y.-A. Chen, T.-C. Chen, P.-J. Chang, Y.-P. Yu, K.-Y. Cheng, C.-H. Shih, G.-H. Lee, H.-S. Sheu, “Synthesis, structure and oxygen-sensing properties of Iridium(iii)-containing coordination polymers with different cations” *Dalton Trans.* **2012**, *41*, 2592.

[15] S. M. Barrett, C. Wang, W. Lin, “Oxygen sensing via phosphorescence quenching of doped metal–organic frameworks” *J. Mater. Chem.* **2012**, *22*, 10329.

[16] R. Xu, Y. Wang, X. Duan, K. Lu, D. Micheroni, A. Hu, W. Lin, “Nanoscale Metal–Organic Frameworks for Ratiometric Oxygen Sensing in Live Cells” *J. Am. Chem. Soc.* **2016**, *138*, 2158–2161.

[17] R. Lin, F. Li, S. Liu, X. Qi, J. Zhang, X. Chen, “A Noble-Metal-Free Porous Coordination Framework with Exceptional Sensing Efficiency for Oxygen” *Angewandte Chemie* **2013**, *125*, 13671–13675.

[18] X.-L. Qi, S.-Y. Liu, R.-B. Lin, P.-Q. Liao, J.-W. Ye, Z. Lai, Y. Guan, X.-N. Cheng, J.-P. Zhang, X.-M. Chen, “Phosphorescence doping in a flexible ultramicroporous framework for high and tunable oxygen sensing efficiency” *Chem. Commun.* **2013**, *49*, 6864.

[19] T. Burger, C. Winkler, I. Dalfen, C. Slugovc, S. M. Borisov, “Porphyrin based metal–organic frameworks: highly sensitive materials for optical sensing of oxygen in gas phase” *J. Mater. Chem. C* **2021**, *9*, 17099–17112.

[20] J. Yang, Z. Wang, Y. Li, Q. Zhuang, J. Gu, “Real-Time Monitoring of Dissolved Oxygen with Inherent Oxygen-Sensitive Centers in Metal–Organic Frameworks” *Chem. Mater.* **2016**, *28*, 2652–2658.

[21] X.-Y. Dong, Y. Si, J.-S. Yang, C. Zhang, Z. Han, P. Luo, Z.-Y. Wang, S.-Q. Zang, T. C. W. Mak, “Ligand engineering to achieve enhanced ratiometric oxygen sensing in a silver cluster-based metal-organic framework” *Nat Commun* **2020**, *11*, 3678.